Arjun Mandal · Subhananda Chakrabarti

Impact of Ion Implantation on Quantum Dot Heterostructures and Devices

Springer

Impact of Ion Implantation on Quantum Dot Heterostructures and Devices

Arjun Mandal · Subhananda Chakrabarti

Impact of Ion Implantation on Quantum Dot Heterostructures and Devices

Springer

Arjun Mandal
Department of Electrical Engineering
Indian Institute of Technology Bombay
Mumbai, Maharashtra
India

Subhananda Chakrabarti
Department of Electrical Engineering
Indian Institute of Technology Bombay
Mumbai, Maharashtra
India

ISBN 978-981-10-4333-8 ISBN 978-981-10-4334-5 (eBook)
DOI 10.1007/978-981-10-4334-5

Library of Congress Control Number: 2017938314

© Springer Nature Singapore Pte Ltd. 2017
This work is subject to copyright. All rights are reserved by the Publisher, whether the whole or part of the material is concerned, specifically the rights of translation, reprinting, reuse of illustrations, recitation, broadcasting, reproduction on microfilms or in any other physical way, and transmission or information storage and retrieval, electronic adaptation, computer software, or by similar or dissimilar methodology now known or hereafter developed.
The use of general descriptive names, registered names, trademarks, service marks, etc. in this publication does not imply, even in the absence of a specific statement, that such names are exempt from the relevant protective laws and regulations and therefore free for general use.
The publisher, the authors and the editors are safe to assume that the advice and information in this book are believed to be true and accurate at the date of publication. Neither the publisher nor the authors or the editors give a warranty, express or implied, with respect to the material contained herein or for any errors or omissions that may have been made. The publisher remains neutral with regard to jurisdictional claims in published maps and institutional affiliations.

Printed on acid-free paper

This Springer imprint is published by Springer Nature
The registered company is Springer Nature Singapore Pte Ltd.
The registered company address is: 152 Beach Road, #21-01/04 Gateway East, Singapore 189721, Singapore

Preface

This monograph reports the findings of a detailed investigation of the impact of ion implantation on the material, electrical and spectral properties of In(Ga)As/GaAs quantum dot (QD) heterostructures.

Over the past two decades, In(Ga)As/GaAs-based QD heterostructures have marked their superiority, particularly for application in lasers and photodetectors. Several in-situ and ex-situ techniques that improve material quality and device performance have already been reported. These techniques are necessary to maintain dot density and dot size uniformity in QD heterostructures and also to improve the material quality of heterostructures by removing defects from a system. While rapid thermal annealing, pulsed laser annealing and the hydrogen passivation technique have been popular as post-growth methods, ion implantation had not been explored largely as a post-growth method for improving the material properties of In(Ga)As/GaAs QD heterostructures. In the present study, we attempted to employ ion implantation as an effective post-growth technique to improve the material properties and, ultimately, the device performance of In(Ga)As/GaAs QD heterostructures. Also, we introduced a capping layer of quaternary alloy InAlGaAs over these In(Ga)As/GaAs QDs to achieve better QD characteristics. With these intensions in mind, the below content had been divided into five chapters as follows: Chap. 1 details the physics of zero-dimensional structures and the electronic properties of QDs. The chapter also discusses different QD fabrication techniques. We address different shortcomings of QDs followed by methods to improve the QD characteristics for In(Ga)As/GaAs QDs. Chapter 2 deals with the impact of both low-energy heavy ion (sulphur) and low-energy light ion (hydrogen) implantations over single-layer InAs/GaAs QDs. The material and structural properties of both un-implanted and implanted QDs are discussed, along with the results achieved through different characterizations. Sulphur (S^-) ion implantation caused degradation of material quality, whereas hydrogen (H^-) ion implantation improved the material properties of InAs/GaAs QDs. In Chap. 3, the structural and optoelectronic properties of quaternary alloy (InAlGaAs)-capped multilayer QD heterostructures were investigated by varying growth rate, capping layer thickness, and seed QD monolayer coverage. In addition, when all the samples were annealed at various

temperatures, the results showed that structural and optoelectronic properties are greatly influenced by annealing temperatures. In Chap. 4, we validate the impact of ion implantation over devices; quaternary alloy-capped InAs/GaAs QDIP devices were implanted with low-energy light ions (H^-). Different steps to fabricate single pixel devices are also discussed in this chapter. A suppression of dark current density was observed for the implanted devices. In Chap. 5, low-energy light ion (H^-) implantations were performed over quaternary alloy-capped InGaAs/GaAs QDIPs. A reduction in dark current density along with enhanced detectivity was measured for the implanted devices.

Mumbai, India

Arjun Mandal
Subhananda Chakrabarti

Acknowledgements

We thank Mr. S.K. Gupta of BARC for his invaluable comments and suggestions towards the betterment of research work. Our heartiest thanks to Dr. P. Singh, Mr. A. Basu, Mr. A. Agarwal and Mr. N.B.V. Subhramanyam of BARC for providing the implantation facility with LEAF and helping out in performing the experiments.

We would like to thank Dr. Shreekumar, Dr. Nilanjan Haldar, Sourav Adhikary, Saumya Sengupta, Kulasekaran M., Hemant Ghadi, Goma Kumari, Aijaz Ahmed, Saikalash Shetty, Akshay Balgarkashi, Harsha Phadke and Jay Agawane for their assistance in fabrication and characterization of the devices. We would like to acknowledge the IRCC Central SPM facility, IIT Bombay, for AFM images. DST, Govt. of India, is being acknowledged for the financial support. We would like to acknowledge MCIT, Government of India, for partial funding through the Centre of Excellence in Nanoelectronics (CEN), IIT Bombay. We also extend our thanks to the European Commission for partial funding through contract SES6-CT-2003-502620 (FULLSPECTRUM).

Contents

1 Introduction to Quantum Dots 1
1.1 Physics of Zero-Dimensional Structures. 1
1.2 Electronic Properties of Quantum Dots 2
1.3 Fabrication of Quantum Dots. 4
1.4 Electronic Spectra of Self-assembled QDs 5
1.5 Disadvantages of Self-assembled QDs 6
1.6 Methods for Improving QD Characteristics 7
1.6.1 Different In-Situ and Ex-Situ Techniques for Improving QD Characteristics 7
1.6.2 Importance of Capping Layers for Improving QD Characteristics 8
1.7 Summary 9
References 10

2 Low-Energy Ion Implantation Over Single-Layer InAs/GaAs Quantum Dots. 13
2.1 Motivation Behind Ion Implantation Study 13
2.2 Scope of the Present Study 14
2.3 Growth of Single-Layer InAs/GaAs QDs. 15
2.4 Ion Implantation and Post-Growth Experiments on QDs 16
2.5 Results and Discussion 16
2.5.1 Structural, Material and Optical Properties of S^- Ion-Implanted InAs/GaAs QDs. 16
2.5.2 Structural, Material and Optical Properties of H^- Ion-Implanted InAs/GaAs QDs. 20
2.6 Conclusions Obtained from the Results of Heavy and Light Ion Implantation on InAs/GaAs QDs. 24
References 25

3 Optimizations for Quaternary Alloy (InAlGaAs)-Capped InAs/GaAs Multilayer Quantum Dots 27
3.1 Motivation Behind the Study 28
3.2 Importance of Multilayer QDs 28
3.3 Growth of Different Quaternary Alloy-Capped Multilayer InAs/GaAs QDs 28
3.4 Post-Growth Experiments Performed on MQDs 30
3.5 Results and Discussion 30
3.5.1 Effects of Variation in Growth Rate of QDs in InAs/GaAs MQD System 31
3.5.2 Impact of Variation in Quaternary Capping Thickness in InAs/GaAs MQD System 33
3.5.3 Effects of Variations in Seed QD Monolayer Coverage for Quaternary Alloy-Capped InAs/GaAs MQDs 33
3.5.4 Effects of Rapid Thermal Annealing (Ex-Situ) on Quaternary Alloy-Capped InAs/GaAs MQDs 34
3.6 Significant Results of Study of Quaternary Alloy-Capped InAs/GaAs MQDs 38
References 39

4 Effects of Low Energy Light Ion (H^-) Implantations on Quaternary-Alloy-Capped InAs/GaAs Quantum Dot Infrared Photodetectors 41
4.1 Introduction: Basic Operation of Intersubband Detectors 41
4.2 Advantages of QDIPs 42
4.3 Previously Reported Results on In(Ga)As/GaAs QDIPs 43
4.4 Growth of Quaternary Alloy-Capped InAs/GaAs QDIPs 44
4.5 Optimization of H^- Ion Fluence and Implantation 45
4.6 Fabrication of Mesa-Shaped Single-Pixel Devices on Implanted Samples 46
4.7 Different Characterizations Performed for Implanted QDIPs 50
4.8 Results and Discussion 50
4.8.1 Optical and Structural Properties of H^- Ion-Implanted InAs/GaAs QDIPs 50
4.8.2 Electrical Properties of H^- Ion-Implanted InAs/GaAs QDIPs 52
4.9 Significant Results from H^- Ion-Implanted InAs/GaAs QDIPs and Conclusions 55
References 55

5 Effects of Low-Energy Light Ion (H^-) Implantation on Quaternary-Alloy-Capped InGaAs/GaAs Quantum Dot Infrared Photodetectors 57
5.1 Scope of the Study 57
5.2 Growth of Quaternary-Alloy-Capped InGaAs/GaAs QDIPs 58

5.3 Ion Implantation, Device Fabrication and Different Characterizations for H^- Ion-Implanted InGaAs/GaAs QDIPs 59
5.4 Results and Discussion 60
5.4.1 Optical Properties of H^- Ion-Implanted InGaAs/GaAs QDIPs 60
5.4.2 Electrical Properties of H^- Ion-Implanted InGaAs/GaAs QDIPs 60
5.5 Significant Results from H^- Ion-Implanted InGaAs/GaAs QDIPs and Conclusions 63
References 64

About the Authors

Dr. Arjun Mandal is currently working as a Research Associate at the University of Wisconsin-Madison, USA. His current work involves GaAs-based hydride vapour-phase epitaxy (HVPE) synthesis of lattice-mismatched "virtual substrates" and materials synthesis for advanced quantum cascade laser (QCL) development. He also works on modelling of vapour-phase epitaxy growths using computational fluid dynamics. Previously, he worked at the Semiconductor Materials and Processes Laboratory (SMPL) at Chonbuk National University, South Korea. During this period, his research works included growth and characterizations of InGaN/GaN quantum dots and multi quantum well (MQW) heterostructures on GaN nanowires for LED device applications. For this purpose, growths were done with nitride-based MOCVD system. Also, he had worked on GaN nanowire–graphene-based hybrid structures for ultraviolet photoconductive device applications. Prior to joining SMPL, he had spent six months in the Electrical Engineering Department, IIT Bombay, as a Research Associate from where he completed his Ph.D. in 2014 in microelectronics; he received his M.Tech. from Institute of Radiophysics and Electronics, University of Calcutta, in 2008. The topic of his doctoral research was effect of ion implantation on the In(Ga)As/GaAs-based quantum dot (QD) heterostructures, mainly infrared photodetectors. He has expertise in molecular beam epitaxy (MBE) system, was responsible for growth optimization and growth of various In(Ga)As/GaAs QD heterostructures over three years during his Ph.D. at IIT Bombay, and also had worked on material and optical characterizations of dots, fabrications and different characterizations of the optoelectronics devices. He had served as a Vice-Chair of IEEE Student Branch, Calcutta section during the period of 2007–2008.

Subhananda Chakrabarti received his M.Sc. and Ph.D. degrees from the Department of Electronic Science, University of Calcutta, Kolkata, India, in 1993 and 2000, respectively. He was a Lecturer in the Department of Physics, St. Xavier's College, Kolkata. He has been a Senior Research Fellow with the University of Michigan, Ann Arbor, from 2001 to 2005; a Senior Researcher with Dublin City University, Dublin City, Ireland, from 2005 to 2006; and a Senior

Researcher (RA2) with the University of Glasgow, Glasgow, UK, from 2006 to 2007. He joined as an Assistant Professor in the Department of Electrical Engineering, IIT Bombay, Mumbai, India, in 2007. Presently, he is a Professor in the same department. He is a Fellow of the Institution of Electrical and Telecommunication Engineers (IETE), India, and also a Member of the IEEE, MRS USA, SPIE USA, etc. He is the 2016 Medal Recipient of the Materials Research Society of India and was also awarded the 2016 NASI-Reliance Industries Platinum Jubilee Award for Application-Oriented Innovations in Physical Sciences. He serves as an Editor of the IEEE Journal of Electron Device Society. He has authored more than 250 papers in international journals and conferences. He has also co-authored a couple of chapters on intersubband quantum dot detectors. His four (4) research monographs with Springer are in press. Dr. S. Chakrabarti serves as a reviewer for a number of international journals of repute such as Applied Physics Letters, Nature Scientific Report, IEEE Photonics Technology Letters, IEEE Journal of Quantum Electronics, Journal of Alloys and Compound and Material Research Bulletin. His research interest lies in compound (III–V and II–VI) semiconductor-based optoelectronic materials and devices.

Abbreviations

0D	Zero-dimensional
1D	One-dimensional
2D	Two-dimensional
3D	Three-dimensional
A	Ampere
Å	Angstrom
AFM	Atomic force microscopy
Al	Aluminium
As	Arsenic
Au	Gold
BARC	Bhabha Atomic Research Centre
cm	Centimetre
D	Detectivity
DC	Direct current
DCXRD	Double-crystal X-ray diffraction
DI	Deionized
DOS	Density of states
FWHM	Full width at half maximum
Ga	Gallium
Ge	Germanium
GeV	Giga electron volt
gm	Gram
G–R	Generation–recombination
H	Hydrogen
HCL	Hydrochloric acid
HF	Hydrogen fluoride
HNO_3	Nitric acid
H_2O	Hydrogen monoxide (water)
H_2O_2	Hydrogen peroxide
H_3PO_4	Phosphoric acid

HRTEM	High-resolution transmission electron microscopy
Hz	Hertz
IIT	Indian Institute of Technology
In	Indium
IPA	Isopropyl alcohol
IR	Infrared
K	Kelvin
keV	Kilo electron volt
kV	Kilo volt
LCC	Leaded chip carrier
LEAF	Low-energy accelerator facility
LN_2	Liquid nitrogen
LO	Longitudinal optical
LWIR	Long-wavelength infrared
MBE	Molecular beam epitaxy
MeV	Mega electron volt
meV	Milli electron volt
mJ	Milli Joules
ML	Monolayer
mm	Millimetre
Mo	Molybdenum
MOCVD	Metal–organic chemical vapour deposition
MQD	Multilayer quantum dot
mW	Milliwatt
MWIR	Mid-wavelength infrared
μm	Micrometre
N	Nitrogen
NaOH	Sodium hydroxide
Ni	Nickel
nm	Nanometre
PL	Photoluminescence
PPR	Positive photo resist
QD	Quantum dot
QDIP	Quantum dot infrared photodetector
QW	Quantum well
QWIP	Quantum well infrared photodetectors
RHEED	Reflection high-energy electron diffraction
S	Sulphur
Sb	Antimony
Si	Silicon
S–K	Stranski–Krastanow
SNICS	Source of negative ion by Caesium sputtering
SNR	Signal-to-noise ratio
STEM	Scanning transmission electron microscopy
TCE	Trichloroethylene

TEM	Transmission electron microscopy
W	Watt
XRD	X-ray diffraction
XTEM	Cross-sectional transmission electron microscopy

List of Figures

Fig. 1.1 Transition of an electron from initial A to final state B after absorbing a photon 3
Fig. 1.2 Atomic force microscopy (AFM) image shows high density of uniform self-assembled InAs/GaAs quantum dots (QDs) grown during the present study 5
Fig. 1.3 Photoluminescence (PL) result shows ground- and excited-state transitions in self-assembled single-layer InAs/GaAs quantum dots (QDs), grown for our research purpose 6
Fig. 2.1 Schematic of single-layer InAs/GaAs quantum dots (QDs) grown on semi-insulating GaAs substrate [11] 15
Fig. 2.2 Atomic force micrographs of InAs/GaAs quantum dots (QDs) **a** un-implanted sample, and **b** sample implanted with 50 keV sulphur ions [11] 17
Fig. 2.3 X-ray diffraction (XRD) patterns from InAs/GaAs quantum dot (QD) heterostructures **a** un-implanted sample; samples implanted with **b** 20 keV, **c** 35 keV, **d** 45 keV and **e** 50 keV sulphur ions [11] 17
Fig. 2.4 Photoluminescence (PL) spectra at 8 K from InAs/GaAs quantum dots (QDs) implanted with sulphur ions of different energies [11] 18
Fig. 2.5 Photoluminescence (PL) spectra at 8 K from InAs/GaAs quantum dots (QDs) implanted with 30 keV sulphur ions of different fluences [11] 19
Fig. 2.6 Variation of integrated PL intensity of ground state with optical excitation density for InAs/GaAs quantum dots (QDs), both for un-implanted sample and sample implanted with 45 keV sulphur ions. Inset shows the variation of ground state PL peak FWHM with energy of sulphur ions [11] 20

Fig. 2.7 X-ray diffraction (XRD) patterns of as-prepared sample and samples implanted with 50 keV H^- ions at different fluences [21]. 21
Fig. 2.8 Variation of full width at half maximum (FWHM) of X-ray reflections from InAs/GaAs quantum dots (QDs) and the GaAs capping layer with different H^- ion fluences [21]. 21
Fig. 2.9 Cross-sectional transmission electron microscopy (XTEM) images of surface dots [21] 22
Fig. 2.10 Photoluminescence (PL) spectra recorded at 8 K with laser excitation density 51.6 W/cm^2 from samples implanted with H^- ions [21]. 23
Fig. 2.11 Photoluminescence (PL) spectra recorded at 8 K with laser excitation density 5 W/cm^2 from the samples implanted with H^- ions [21]. 23
Fig. 2.12 Variation of integrated PL intensity with laser excitation density for H^- ion-implanted InAs/GaAs quantum dots (QDs) [21] 24
Fig. 3.1 Heterostructure of the multilayer quantum dot (MQD) sample as specified in Table 3.1 [21]. 29
Fig. 3.2 Transmission electron microscopy (TEM) images of **a** sample A1, **b** sample A2, **c** sample B1, **d** sample B2 and **e** sample B3 [21]. 30
Fig. 3.3 Comparison of low-temperature photoluminescence (PL) of all as-grown multilayer quantum dot (MQD) samples giving an approximation of their emission peaks [21] 31
Fig. 3.4 Excitation-power-dependent photoluminescence (PL) plot of sample A1 demonstrating number of quantum dot (QD) families [21] 32
Fig. 3.5 Excitation-power-dependent photoluminescence (PL) results of sample A2 demonstrating number of quantum dot (QD) families [21]. 32
Fig. 3.6 Temperature-dependent integrated photoluminescence (PL) intensity plot of as-grown samples B1, B2 and B3 [21]. . . . 34
Fig. 3.7 Photoluminescence (PL) spectra depicting the thermal stability of sample A1 for different annealing temperatures [21] 35
Fig. 3.8 Photoluminescence (PL) spectra depicting thermal stability of sample A2 for different annealing temperatures [21] 35
Fig. 3.9 Transmission electron microscopy (TEM) image of sample A2 annealed at 800 °C, depicting the degradation of quantum dots (QDs) at high temperatures [21]. 35

Fig. 3.10 Power-dependent photoluminescence (PL) spectra of sample A2 **a** annealed at 650 °C, depicting two quantum dot (QD) families, and **b** annealed at 700 °C, depicting three quantum dot families [21] 36
Fig. 3.11 Low-temperature photoluminescence (PL) spectra for annealed **a** sample B2 and **b** sample B3 [21] 37
Fig. 3.12 Low-temperature photoluminescence (PL) spectra for annealed sample B1 [21] 37
Fig. 3.13 Transmission electron microscopy (TEM) image of sample B2 annealed at 750 °C [21] 38
Fig. 4.1 Basic heterostructures of quantum well and quantum dot infrared photodetectors (QWIPs and QDIPs) 42
Fig. 4.2 Schematic structure of an InAs/GaAs quantum dot infrared photodetector (QDIP) and a simplified band diagram to show its basic operation 43
Fig. 4.3 Heterostructure of quaternary-alloy-capped 8-layered n-i-n InAs/GaAs quantum dot infrared photodetector (QDIP) [24] 45
Fig. 4.4 Heterostructure of quaternary-alloy (InAlGaAs) capped single-layer InAs/GaAs quantum dot (QD) used for optimizing fluence of H^- ion implantation 45
Fig. 4.5 Room-temperature photoluminescence (PL) peaks from quaternary-alloy-capped single-layer InAs/GaAs quantum dot (QD) heterostructures implanted with 50 keV H^- ions of fluence varying between 7×10^{11} and 6×10^{12} ions/cm^2. . . . 46
Fig. 4.6 Heterostructure of a single-pixel device after fabrication 47
Fig. 4.7 Picture taken after mesa lithography of devices 47
Fig. 4.8 After wet etching, the structures are ready for contact definition 48
Fig. 4.9 Picture taken after contact lithography during device fabrication 48
Fig. 4.10 Prominent mesa-shaped single-pixel devices after metallization 49
Fig. 4.11 Contacts of devices are wire bonded with leaded chip carrier (LCC) pad 50
Fig. 4.12 Photoluminescence (PL) comparisons at 8 K for as-grown and implanted quaternary alloy capped InAs/GaAs quantum dot infrared photodetectors (QDIPs) [24] 51
Fig. 4.13 Photoluminescence (PL) comparisons at 8 K for as-grown and implanted samples at the lowest excitation power of 500 μW [24] 51
Fig. 4.14 Atomic force microscopy (AFM) image of quaternary-alloy-capped single-layer InAs/GaAs quantum dots to study surface morphology. The *black spotted dots* are larger in size [24] 52

Fig. 4.15 Variation of full width at half maximum (FWHM) of photoluminescence (PL) emission with implantation (fluence values of 50 keV H^- ions) for smaller and larger dot families [24] 53
Fig. 4.16 Different sources of dark current generation: thermionic emission (**a**), field-assisted tunnelling (**b**), sequential tunnelling (**c**) and thermally assisted tunnelling (**d**) [24] 53
Fig. 4.17 Variation of dark current density with bias at 77 K for the as-grown and implanted InAs/GaAs quantum dot (QD) detectors [24] 53
Fig. 4.18 Variation of activation energies at both positive and negative bias for the as-grown and implanted InAs/GaAs quantum dot (QD) detectors at 77 K [24]. 54
Fig. 5.1 Room temperature photoluminescence emissions from single-layer quaternary-alloy-capped InGaAs and InAs quantum dots (QDs), grown for our research purpose 58
Fig. 5.2 Heterostructure of ten-layered quaternary alloy (InAlGaAs) capped $In_{0.5}Ga_{0.5}As$/GaAs quantum dot infrared photodetector (QDIP) [1] 59
Fig. 5.3 Room temeprature photoluminescence (PL) emissions from as-grown and implanted InGaAs/GaAs quantum dot infrared photodetectors (QDIPs) 60
Fig. 5.4 Low-temperature (77 K) dark current density comparison of as-grown and implanted devices show decrease in dark current density of up to five orders for device C as compared to device A [1]. 61
Fig. 5.5 Activation energy calculated at zero bias from temperature-dependent *I*–*V* measurements for as-grown device A increased up to device C [1] 62
Fig. 5.6 At a low bias of −0.1 V and low temperature of 77 K, a stronger multicolour photo-response was achieved from device B. The inset shows that the peak intensity ratio of the mid-wavelength response (P1) to the long-wavelength response (P2) is highest for device B [1]. 62
Fig. 5.7 Increase in peak detectivity (D*) by more than one order for device B at a temperature of 87 K and a bias of 0.3 V [1] 63

List of Tables

Table 3.1 Specifications of basic heterostructure of various InAlGaAs-capped multilayer InAs/GaAs quantum dot (QD) heterostructures. 29
Table 5.1 Implanted fluences and nomenclature for as-grown and implanted InGaAs/GaAs quantum dot infrared photodetectors (QDIPs) 59

Chapter 1
Introduction to Quantum Dots

Abstract This chapter deals with the basics of zero-dimensional quantum structures, i.e. quantum dots. An abridged explanation of its electronic properties is mentioned in this chapter. Different fabrication techniques for growing quantum dots are also chalked out in short. The advantages and disadvantages of self-assembled quantum dots are described in detail. Various in-situ and ex-situ techniques along with importance of different capping layers for improving electronic properties of self-assembled quantum dots are also referred in this chapter.

Keywords Self-assembled quantum dots (QDs) · Electronic properties · Zero-dimensional structures · In-situ and ex-situ techniques · Capping layers

1.1 Physics of Zero-Dimensional Structures

Quantum dots (QDs) are semiconductor structures with dimensions smaller than the de Broglie wavelength [1]. The dimensionality in nanoscale structures refers to the number of directions in which carriers inside a material can act as free carriers. When the movement of the carriers is constrained by potential barriers, the degree of freedom may be reduced to two, one or zero dimensions. For a bulk 3D (three-dimensional) structure, electronic carriers can act freely in all three directions. When the bulk material is spatially confined in one direction, carriers inside would therefore be free only in two directions, this gives rise to a 2D (two-dimensional) structure, also known as a quantum well (QW). Taking this spatial confinement a step further, a 1D (one-dimensional) structure quantum wire is produced by limiting the spatial motion of carriers to a single dimension. Finally, if the material is spatially confined in all three directions, a 0D (zero-dimensional) structure, also known as quantum dot, is formed [2].

The critical parameter for size confinement in semiconductor nanoscale materials is exciton Bohr diameter, which is used to evaluate the size condition for creating the quantum confinement effect. Bohr diameter is the natural distance in a crystal between an electron in the conduction band and its corresponding hole in the

© Springer Nature Singapore Pte Ltd. 2017

A. Mandal and S. Chakrabarti, *Impact of Ion Implantation on Quantum Dot Heterostructures and Devices*, DOI 10.1007/978-981-10-4334-5_1

valence band. In a 3D structure, the dimension of the semiconductor crystal is larger than the exciton Bohr diameter. Thus, an exciton is extended to its natural limit in bulk material, and electron energy levels are continuous. However, if we allow as the semiconductor crystal size approaches the size of a material's Bohr diameter, the electron energy levels become discrete, which is called quantum confinement. If these conditions are fulfilled in all three directions, a semiconductor material becomes a quantum dot [2, 3].

1.2 Electronic Properties of Quantum Dots

As mentioned in the preceding section, QDs exhibit complete discrete energy levels within the conduction band and valance band due to three-dimensional confinement. Let us consider a simple quantum box with dimensions L_x, L_y and L_z. Here, we focus on the conduction band. The wave function and energy state of a box-shaped QD (by solving Schrödinger's equation) are given in Eqs. 1.1 and 1.2, respectively [2]:

$$\Psi_{\mathrm{c,nlm}} = \left[\frac{2}{L}\right]^{3/2} \sin\left[\frac{n\pi}{L_x}x\right] \sin\left[\frac{l\pi}{L_y}y\right] \sin\left[\frac{m\pi}{L_z}z\right] U_{\mathrm{c}}(\vec{r}), \tag{1.1}$$

$$E_{\mathrm{c,nlm}} = E_C + \frac{\hbar^2\pi^2}{2m_{\mathrm{c}}^* L_x^2}n^2 + \frac{\hbar^2\pi^2}{2m_{\mathrm{c}}^* L_y^2}l^2 + \frac{\hbar^2\pi^2}{2m_{\mathrm{c}}^* L_z^2}m^2, \tag{1.2}$$

where, n, l, m = 1, 2, 3 …., $U_{\mathrm{c}}(\vec{r})$ is the wave function of a unit cell, and m_{c}^* is the effective mass of electrons in the conduction band. Three-dimensional quantum confinement splits the conduction band into atomic-like discrete energy levels. For this reason, quantum dots are also known as "artificial atoms". The energy separation between these energy levels depends on the dimensions of the quantum box.

The atomic-like discrete energy levels show a delta-function-like density of states (DOS), $\rho_{\mathrm{QD}}(E)$, which can be written as:

$$\rho_{\mathrm{QD}}(E) = g(E_n)\,\delta\,(E - E_n), \tag{1.3}$$

where $g(E_n)$ is the degeneracy of the energy level E_n. Reference [3] depicts density of states for bulk materials, quantum wells, quantum wires and quantum dots.

The atomic-like discrete energy levels in QDs have a longer excited-state lifetime. We know that non-radiative relaxation is caused by the thermally activated electron-longitudinal optical (LO) phonon scattering process [4] in quantum structures. In a quantum well structure, the energy states are quantized only along the growth direction (z direction) while the in-plane energy states are quasi-continuous. These quasi-continuous energy states make it easy to achieve resonant electron-LO phonon scattering. The LO-scattering nonradiatively

depopulates electrons from the upper states to the lower states much faster (2300 times) than radiative emission processes [5, 6]. Such a fast non-radiative relaxing rate leads to a short excited-state lifetime. In quantum dots, since discrete energy levels are not resonant with LO phonons, LO phonon-related non-radiative relaxation can be substantially reduced, leading to a long excited-state lifetime. This is typically referred to as the "phonon bottleneck" effect [7, 8]. The long excited-state lifetime leads to better quantum efficiency, which eventually helps overcome the effects of low fill factor (20–25%) of QDs [9].

The above-mentioned QD properties are the primary reasons for their applications in intersubband detection [10]. Due to photon absorption, the transition rate for an electron initially at state A and finally at state B (Fig. 1.1) can be written using Fermi's golden rule [11] as follows:

$$w_{\mathrm{BA}} = \frac{2\pi}{\hbar} |\langle \psi_{\mathrm{B}} | H' | \psi_{\mathrm{A}} \rangle|^2 \delta(E_{\mathrm{B}} - E_{\mathrm{A}} - \hbar\omega), \tag{1.4}$$

where ψ_{A} and ψ_{B} are the wave functions at the subbands, and H' is the interaction Hamiltonian of the incident light with QDs.

Further, the interaction Hamiltonian can also be written using electric dipole approximation as [12]:

$$H' = -e\vec{r} \cdot \vec{E}, \tag{1.5}$$

where, $-e\vec{r}$ is the electric dipole moment and $\vec{E}$ is the electric field.

Also, from the quantum selection rule for intersubband transitions [13], we know the nonzero matrix element $H'_{\mathrm{BA}} = \langle \psi_{\mathrm{B}} | H' | \psi_{\mathrm{A}} \rangle \neq 0$. For normal incidence in z direction, the electric field is along the x- or y-direction. Assuming $\vec{E}$ is along the x-direction, for the simple quantum box example, the matrix element $\mathrm{H}'_{\mathrm{BA}}$ can be written as:

$$H'_{\mathrm{BA}} = \langle \psi_{\mathrm{B}} | - exE | \psi_{\mathrm{A}} \rangle = C \left\langle \sin\left[\frac{B\pi}{L_x} x\right] \middle| - exE \middle| \sin\left[\frac{A\pi}{L_x} x\right] \right\rangle, \tag{1.6}$$

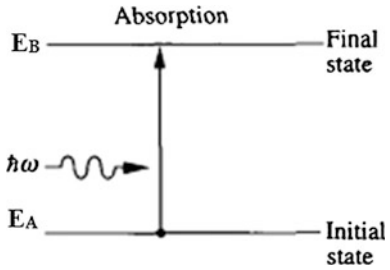

Fig. 1.1 Transition of an electron from initial A to final state B after absorbing a photon

where C is a constant containing the integration of unit cell wave function $U_c(\vec{r})$. Again, due to the quantization in the x- and y-directions for a QD box, ψ_A and ψ_B are functions in x and y; thus, there exists a nonzero matrix element H'_{BA}, indicating normal incidence absorption and detection capability [13].

1.3 Fabrication of Quantum Dots

Several techniques had been developed for quantum dot fabrication in the past two decades. Some of these techniques used the semiconductor quantum well as the starting point. Electron beam lithography and etching can be performed on quantum well to obtain free-standing nano-pillar structures [14]. Another method involves evaporating an array of small electrodes onto this quantum well surface. When these electrodes are polarized with voltage, the resulting electrostatic fields propagate down to the quantum well layers and create lateral confinement. Further, selective intermixing of quantum well and barrier materials has been used in conjunction with pulsed laser annealing and ion implantation [14]. The intermixing of well and barrier materials at the implanted or illuminated spot led to variation in quantum well thickness, resulting in quantum dots. We can also fabricate quantum dots by selective epitaxy, using lithography and a mask to deposit quantum dot materials.

As mentioned in the previous section, the electron energy levels of QDs are discrete rather than continuous. Hence, there is always the option of tailoring the band gap by engineering the size of the QDs as per the desired application; i.e. the optical properties of a QD material can be modelled. However, the above-mentioned fabrication techniques produce quantum dots of varying shape and size, which is inappropriate for optoelectronic devices as they always require a high density of uniform and defect-free QDs. Too big a dot size prevents three-dimensional quantum confinement, while too small a dot size hinders the formation of localized states. For example, the optimum width of InAs/GaAs QD is 4–20 nm [3].

In the present study, growth of uniform and defect-free QDs at high density was realized using crystal growth techniques such as molecular beam epitaxy (MBE) and metal–organic chemical vapour deposition (MOCVD). The QDs grown by these techniques are self-assembled QDs. Self-assembled QD structures have now become a well-accepted approach and are widely used in III–V semiconductor systems. Different growth modes for self-assembled QDs are particularly based on the selection of materials, their lattice mismatch and the presence of strain [14] in the QD system. For example, when highly strained In(Ga)As is epitaxially grown on the lattice-mismatched GaAs substrate in the so-called Stranski–Krastanow (SK) growth mode [3], self-assembled islands (QD structures) are formed after a few monolayers (ML) of layer-by-layer growth (called a wetting layer). Figure 1.2 shows an atomic force microscopy (AFM) image of a single-layer InAs/GaAs QD structure grown by MBE. Here, the dot density is of the order of 10^{10} dots/cm^2.

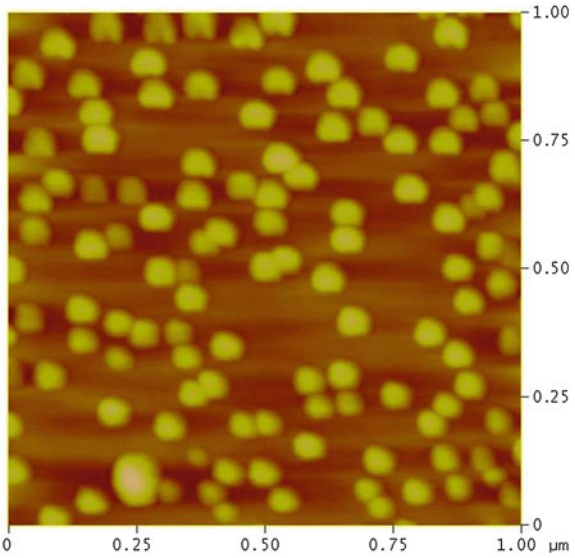

Fig. 1.2 Atomic force microscopy (AFM) image shows high density of uniform self-assembled InAs/GaAs quantum dots (QDs) grown during the present study

The advantage of this self-assembled process is that further etching, annealing or implantation processes are avoided. Since the dots are self-organized, a homogeneous surface morphology is maintained. However, due to presence of strain in the heterostructures, strain-related defects and dislocations cannot be avoided entirely.

1.4 Electronic Spectra of Self-assembled QDs

The presence of strain in the self-assembled QD structures impacts the electronic properties of QDs by changing the energy levels of the localized carriers and their wave functions [15]. Jiang's study using the eight-band $k \cdot p$ model [16] provides a good understanding of the electronic spectra of self-assembled QDs. Jiang calculated the electronic spectra considering an InAs/GaAs QD system. In this study, the QD structure is assumed to be pyramidal in shape, with a base width of 113 Å, a height of 56.5 Å and a wetting layer thickness of 1.5 ML.

These results show that there are a number of discrete excited states in the conduction band along with a mixture of less confined wetting layer states. It can be observed that the separation between the bound ground electron states is larger than the optical phonon energy in the dot material ($\sim$36 meV); therefore, optical phonon scattering is suppressed in the QD system and a phonon bottleneck exists [7, 8]. The room-temperature photoluminescence (PL) spectrum of self-assembled InAs/GaAs QDs is shown in Fig. 1.3. The PL spectrum depicts ground- and excited-state transitions in self-assembled QDs.

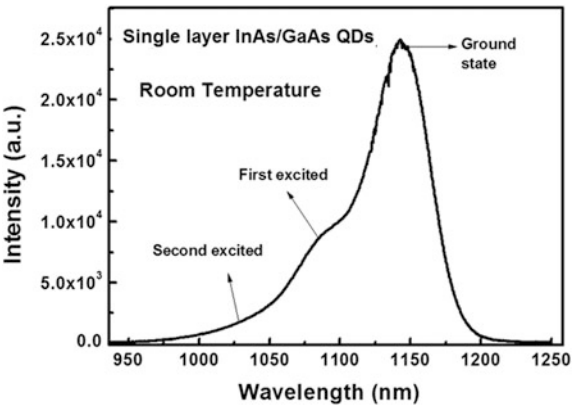

Fig. 1.3 Photoluminescence (PL) result shows ground- and excited-state transitions in self-assembled single-layer InAs/GaAs quantum dots (QDs), grown for our research purpose

1.5 Disadvantages of Self-assembled QDs

As we know, formation of dots with random size variations cannot be controlled during the self-assembly growth process; i.e. the homogeneity and uniformity of dots cannot be maintained minutely throughout the QD matrix. This is the main disadvantage of self-assembled QDs. Due to this size variation of dots, an unwanted shift occurs in the emission spectra of dots, which is detrimental for optoelectronic applications. Also, during the growth of buried self-assembled QDs on lattice-mismatched substrates, stress relaxation process in QDs results in the formation of misfit dislocations at the interface of a dot and the barrier layer [15]. For these strained QDs, relaxation processes start, and additional defects form, when the dot size increases beyond a critical threshold. These additional defects include non-radiative recombination centres and point and extended defects. Formation of these additional defects and dislocations at the QD vicinity or dot–barrier layer interface actually modifies the physical properties of the material. These modifications, which are attributed to defect formation within the QD structures, ultimately lead to the degradation of material quality and eventually affect device performance [15].

Moreover, for stacked self-assembled multilayer QD (MQD) structures, two kinds of strain are present in the systems: an overall homogeneous strain and a localized inhomogeneous strain [17]. These MQD structures are mainly grown with III–V compound semiconductors, e.g. InAs/GaAs MQD structures. The homogeneous strain is present throughout the multilayered structure, but starts at the interface and propagates uniformly through the barrier layer and the multiple QD layers in the active region, thereby producing the effect of a cumulative strain. In contrast, the inhomogeneous strain is localized at a particular QD island. The cumulative strain leads to the generation of threading dislocations in the MQD structure throughout the stacking, which results in non-uniform and inhomogeneous dot density for the upper layer of dots [18].

1.6 Methods for Improving QD Characteristics

1.6.1 Different In-Situ and Ex-Situ Techniques for Improving QD Characteristics

Many in-situ and ex-situ techniques are available in literature for improving the QD characteristics. In the present study, we will mainly discuss In(Ga)As/GaAs QD heterostructures. Normally, the growth conditions of a In(Ga)As/GaAs quantum dot layer determine parameters such as dot density, homogeneity and original size of quantum dots [19]. For multilayer In(Ga)As/GaAs QD heterostructures, the threading dislocation problem may be addressed by overgrowing the GaAs barrier layer up to an appropriate thickness. A thick barrier layer can suppress the cumulative strain and thus provides a smooth surface for the growth of subsequent QD layers [17, 20]. Many researchers also apply in-situ annealing or growth pause during the growth of the QDs; however, these are not effective techniques for improving QD quality, and QD characteristics may instead degrade [21, 22].

Different post-growth or ex-situ methods such as rapid thermal annealing, pulsed laser annealing and passivation are also very popular for improving QD characteristics. Hydrogen passivation [23] and nitrogen exposure [24] on an InAs/GaAs QD system improve the material quality of dots by reducing the defects in the system. Chakrabarti et al. [25] showed that the material properties of an InAs/GaAs QD system could be improved with pulsed laser annealing of the point and extended defects in and around the dots. Rapid thermal annealing is also an effective method of eradicating defects from the In(Ga)As/GaAs QD system and ultimately improving material quality and device performance [26]. However, ex-situ annealing of the InAs/GaAs QD system leads to In-Ga interdiffusion, which results in the blue shift of emission spectra. We therefore need to develop a post-growth method that can improve QD properties without changing physical dimensions.

Ion implantation is a relatively less explored post-growth method known to improve the material characteristics of dots. This research work focuses on the impact of ion implantation on In(Ga)As/GaAs QD materials and devices. Leon et al. demonstrated slight enhancement of PL emission at 5 K using 1.5 meV proton implantation on single-layer InGaAs/GaAs QDs [27, 28]. Later, Lu and co-workers demonstrated enhancement of PL efficiency in multilayer InAs QDs on proton implantation (50–70 keV) followed by rapid thermal annealing at 700 °C [29, 30]. These two are among the best results available in literature regarding the improvement of material properties of In(Ga)As/GaAs QDs through ion implantation. In this work, both heavy and light ions were implanted over In(Ga)As/GaAs QDs, and the material properties of both un-implanted and implanted QDs were studied. To validate the effects of ion implantation on material properties, and ultimately to check the impact on devices, fabrication and characterization of devices were performed both with and without ion implantation.

1.6.2 *Importance of Capping Layers for Improving QD Characteristics*

As discussed earlier, over the past two decades, self-assembled In(Ga)As quantum dots grown on GaAs substrates are of great interest because of their potential applications in lasers and intersubband detectors [31]. Although dot density and homogeneity are mainly determined by growth conditions, capping the dots modulates the final properties of quantum dots as it redistributes the atoms [19], which is responsible for changes in dot shape. Moreover, the variation of strain field surrounding the dots during the capping process is attributed to the composition and thickness of the layers grown above the QDs. The most common types of capping layers studied extensively so far for InAs dots are the simple GaAs capping layer, InGaAs and GaAsSb capping layers [19] and the quaternary alloy InAlGaAs capping layer. The advantages and disadvantages of these capping layers are discussed below.

1.6.2.1 Use of GaAs Capping Layer

InAs dots are formed in Stranski–Krastanow growth mode [3] to decrease the strain in deposited InAs material. The lowest strain persists at the apex of a quantum dot [19]. As we know, InAs has a higher lattice constant than GaAs [32]. When InAs dots are capped by a GaAs layer, the compressive strain inside dots is further increased [33], which in turn prevents achieving longer emission wavelength. Also, Hazdra et al. [34] showed that both increase of compressive strain inside InAs dots and reduction of tensile strain in the GaAs capping layer are responsible for the blue shift of the ground-state emission of GaAs-capped InAs dots. The emission wavelength of InAs quantum dots capped with GaAs is usually around 1200 nm at room temperature. However, application of these InAs/GaAs QDs in telecommunication devices requires emission wavelengths of 1300 or 1550 nm [19]. This is the main disadvantage of using a GaAs capping layer for InAs dots.

1.6.2.2 InGaAs and GaAsSb as Strain-Reducing Capping Layers

To overcome the problems with GaAs capping layer mentioned in the preceding section and to shift the emission wavelength to 1300 or 1550 nm, as necessary for optical fibre communication [19], we must employ other capping layers that can reduce the strain further inside the dots. For that purpose, the most popular capping layers available in literature are InGaAs [35, 36] and GaAsSb [37, 38]. Both these capping layers help in reducing dot deformation, releasing the strain inside the dots and decreasing the barrier energy for electrons and holes [19]. Moreover, an InGaAs capping layer helps in accumulation of indium (In) atoms in the vicinity of

InAs dots, and thus increasing dot size. Increase in dot size also leads to the red shift of the emission wavelength [19].

However, use of InGaAs capping for InAs QDs poses a particular disadvantage in case of laser applications. Very small energy separation exists between the ground and excited states of the dots because of the lower energy barriers and the increased dot size due to InGaAs capping [19]. Therefore, lasing usually starts from the excited states with higher DOS, and not from the ground states. Thus, the emission wavelengths get shortened. In contrast, use of GaAsSb capping layer provides comparatively higher energy barriers [19], and thus, the problem posed by InGaAs capping can be avoided. Conversely, GaAsSb capping does not allow In gathering in dot vicinity, and so the red shift we achieve with GaAsSb capping is not as strong as with InGaAs capping [19].

1.6.2.3 Importance of Quaternary Alloy (InAlGaAs) Capping

Although some of best results were obtained for In(Ga)As/GaAs QDs with InAlGaAs capping [39], this method has not been used extensively so far. In this research work, we further explored how this quaternary capping improved the material quality and device performance for In(Ga)As/GaAs QD systems. The quaternary $In_{0.21}Al_{0.21}Ga_{0.58}As$ capping used in QDs functions as a strain-driven phase separation alloy [40]. As a result of variation in the inhomogeneous surface strain over a QD layer, the In atoms from the quaternary InAlGaAs alloy diffuse into the vicinity of dots near the elastically relaxed region, thereby forming an In concentration gradient along the periphery of the QD islands. This concentration gradient helps in preventing the out-diffusion of In atoms from the dots during the growth of the capping layer [40]. This is the main advantage of using this quaternary capping.

However, the diffusion of In atoms from the quaternary alloy into the elastically relaxed regions of the dots leads to alloy surface distortion and roughness, rendering it useless for the growth of subsequent QD layers [18], and also leads to the generation of threading dislocations in the QD structure. This quaternary capping is then overgrown with an intrinsic GaAs layer of appropriate thickness. The composition $In_{0.21}Al_{0.21}Ga_{0.58}As$ for this alloy is almost lattice-matched with GaAs. Thus, the Ga adatoms from GaAs layer can fill-in the surface roughness of the quaternary alloy and make the growth front uniform [17].

1.7 Summary

Basic semiconductor physics for zero-dimensional quantum structures, i.e. QDs, had been explained along with its electronic properties. Different fabrication techniques for QDs are also mentioned. A detailed study on the advantages and

disadvantages of self-assembled QDs had been made, whereas important in-situ and ex-situ techniques during and after the growth of QDs are also explained elaborately for improving QD properties. The significant method of using various capping layers for the advancement of QD (In(Ga)As/GaAs QDs) properties is also discussed.

References

1. M. Asada, Y. Miyamoto, Y. Suematsu, Gain and the threshold of three-dimensional quantum-box lasers. Quantum Electron., IEEE J. **22**, 1915–1921 (1986)
2. Paul Harrison, *Quantum Wells, Wires and Dots—Theoretical and Computational Physics of Semiconductor Nanostructures* (Wiley, Chichester, U.K., 2005)
3. Mitsuru Sugawara, *"Self-assembled InGaAs/GaAs Quantum Dots", Semiconductors and Semimetals*, vol. 60 (Academic Press, New York, USA, 1999)
4. B.S. Williams, H. Callebaut, S. Kumar, Q. Hu, J.L. Reno, 3.4-THz quantum cascade laser based on longitudinal-optical-phonon scattering for depopulation. Appl. Phys. Lett. **82**, 1015–1017 (2003)
5. F. Jerome, F. Capasso, C. Sirtori, D. Sivco, A. Hutchinson, A. Cho, Quantum Cascade Laser. Science **264**, 553–556 (1994)
6. C.-F. Hsu, O. Jeong-Seok, P. Zory, D. Botez, Intersubband quantum-box semiconductor lasers. Sel. Topics Quantum Electron, IEEE J. **6**, 491–503 (2000)
7. U. Bockelmann, G. Bastard, Phonon scattering and energy relaxation in two, one, and zero-dimensional electron gases. Phys. Rev. B **42**, 8947 (1990)
8. H. Benisty, C. Sotomayor-Torres, C. Weisbuch, Intrinsic mechanism for the poor luminescence properties of quantum-box systems. Phys. Rev. B **44**, 10945 (1991)
9. A. Mandal, A. Agarwal, H. Ghadi, Goma Kumari K.C., A. Basu et al., "More than one order enhancement in peak detectivity (D*) for quantum dot infrared photodetectors implanted with low energy light ions (H^-)," Applied Physics Letters, vol. 102, pp. 051105 (2013)
10. Jasprit Singh, *Electronic and Optoelectronic Properties of Semiconductor Structures* (Cambridge University Press, New York, USA, 2003)
11. Shun Lien Chuang, *Physics of Photonic Devices* (Wiley, New Jersey, USA, 2009)
12. D.A.B. Miller, *Quantum Mechanics for Scientists and Engineers* (Cambridge University Press, New York, USA, 2008)
13. Manijeh Razeghi, *Technology of Quantum Devices* (Springer, New York, USA, 2010)
14. D. Bimberg, M. Grundmann, N.N. Ledentsov, *Quantum Dot Heterostructures* (Wiley, Chichester, U.K., 1999)
15. Zhiming M. Wang, *Self-assembled Quantum Dots* (Springer, New York, USA, 2008)
16. Hongtao Jiang, Jasprit Singh, Strain distribution and electronic spectra of InAs/GaAs self-assembled dots: An eight-band study. Phys. Rev. B **56**, 4696–4701 (1997)
17. J. Tatebayashi, N. Nuntawong, P.-S. Wong, Y. Xin, L. Lester, D. Huffaker, Strain compensation technique in self-assembled InAs/GaAs quantum dots for applications to photonic devices. J. Phys. D Appl. Phys. **42**, 073002 (2009)
18. G. Solomon, J. Trezza, A. Marshall, J. Harris, JS, 'Vertically aligned and electronically coupled growth induced InAs islands in GaAs". Phys. Rev. Lett. **76**, 952–955 (1996)
19. Ameenah Al-Ahmadi, *Quantum Dots—A Variety of New Applications* (InTech, Croatia, 2012)
20. J. Suseendran, N. Halder, S. Chakrabarti, T. Mishima, C. Stanley, Stacking of multilayer InAs quantum dots with combination capping of InAlGaAs and high temperature grown GaAs. Superlattices Microstruct. **46**, 900–906 (2009)

21. N. Halder, R. Rashmi, S. Chakrabarti, C.R. Stanley, M. Herrera, N.D. Browning, A comprehensive study of the effect of in situ annealing at high growth temperature on the morphological and optical properties of self assembled InAs/GaAs QDs. Appl. Phys. A: Mater. Sci. and Process. **95**, 713–720 (2009)
22. S. Sengupta, N. Halder, S. Chakrabarti, Investigation of effect of varying growth pauses on the structural and optical properties of InAs/GaAs quantum dots heterostructure. Superlattices Microstruct. **46**, 611–617 (2009)
23. E.C. Le Ru, P.D. Siverns, R. Murray, Luminescence enhancement from hydrogen-passivated self-assembled quantum dots. Appl. Phys. Lett. **77**, 2446–2448 (2000)
24. G. Sasikala, I. Suemune, P. Thilakan, H. Kumano, K. Uesugi, Y. Nabetani, T. Matsumoto, H. Machida, "Structural and Luminescence Properties of InAs Quantum Dots: Effect of Nitrogen Exposure on Dot Surfaces," Japanese J. Appl. Phys., vol. 44, pp. L 1512–L 1515 (2005)
25. S. Chakrabarti, S. Fathpour, K. Moazzami, J. Phillips, Y. Lei, N. Browning et al., Pulsed laser annealing of self-organized InAs/GaAs quantum dots. J. Electron. Mater. **33**, L5–L8 (2004)
26. S. Adhikary, S. Chakrabarti, A detailed investigation on the impact of post-growth annealing on the materials and device characteristics of 35-layer $In_{0.50}Ga_{0.50}As$/GaAs quantum dot infrared photodetector with quaternary $In_{0.21}Al_{0.21}Ga_{0.58}As$ capping. Mater. Res. Bull. **47**, 3317–3322 (2012)
27. R. Leon, G. Swift, B. Magness, W. Taylor, Y. Tang, K. Wang et al., Changes in luminescence emission induced by proton irradiation: InGaAs/GaAs quantum wells and quantum dots. Appl. Phys. Lett. **76**, 2074–2076 (2000)
28. R. Leon, S. Marcinkecius, J. Siegert, B. Cechavicius, B. Magness, W. Taylor et al., Effects of proton irradiation on luminescence emission and carrier dynamics of self-assembled III-V quantum dots. Nucl. Sci., IEEE Trans. **49**, 2844–2851 (2002)
29. W. Lu, Y. Ji, G. Chen, N. Tang, X. Chen, S. Shen et al., Enhancement of room-temperature photoluminescence in InAs quantum dots. Appl. Phys. Lett. **83**, 4300–4302 (2003)
30. Y. Ji, G. Chen, N. Tang, Q. Wang, X. Wang, J. Shao et al., Proton-implantation-induced photoluminescence enhancement in self-assembled InAs/GaAs quantum dots. Appl. Phys. Lett. **82**, 2802–2804 (2003)
31. P. Bhattacharya, Z. Mi, Quantum-dot optoelectronic devices. Proc. IEEE **95**, 1723–1740 (2007)
32. Christian Gilfert, Johann Peter P. Reithmaier, "Semiconductor Lasers for Sensor Applications," Nanotechnological Basis for Advanced Sensors, NATO Science for Peace and Security Series B: Physics and Biophysics, pp. 333–353, (2011)
33. H.B. Wu, S.J. Xu, J. Wang, Impact of the cap layer on the electronic structure and optical properties of self-assembled InAs/GaAs quantum dots. Phys. Rev. B **74**, 205329 (2006)
34. P. Hazdra, J. Oswald, V. Komarnitskyy, K. Kuldová, A. Hospodková, E. Hulicius, J. Pangrác, Influence of capping layer thickness on electronic states in self assembled MOVPE grown InAs quantum dots in GaAs. Superlattices Microstruct. **46**, 324–327 (2009)
35. V.D. Dasika, J.D. Song, W.J. Choi, N.K. Cho, J.I. Lee, R.S. Goldman, Influence of alloy buffer and capping layers on InAs/GaAs quantum dot formation. Appl. Phys. Lett. **95**, 163114 (2009)
36. J.S. Kim, J.H. Lee, S.U. Hong, W.S. Han, H.-S. Kwack, C.W. Lee, D.K. Oh, Manipulation of the structural and optical properties of InAs quantum dots by using various InGaAs structures. J. Appl. Phys. **94**, 6603–6606 (2003)
37. V. Haxha, I. Drouzas, J.M. Ulloa, M. Bozkurt, P.M. Koenraad, D.J. Mowbray, H.Y. Liu, M. J. Steer, M. Hopkinson, M.A. Migliorato, Role of segregation in InAs/GaAs quantum dot structures capped with GaAsSb strain-reduction layer. Phys. Rev. B **80**, 165331 (2009)
38. J.M. Ulloa, W.D.I. Drouzas, P.M. Koenraad, D.J. Mowbray, M.J. Steer, H.Y. Liu, M. Hopkinson, Suppression of InAs/GaAs quantum dot decomposition by the incorporation of a GaAsSb capping layer. Appl. Phys. Lett. **90**, 213105 (2007)

39. S. Chakrabarti, S. Adhikary, N. Halder, Y. Aytac, and A. Perera, "High-performance, long-wave ($\sim$ 10.2 μm) InGaAs/GaAs quantum dot infrared photodetector with quaternary $In_{0.21}Al_{0.21}Ga_{0.58}As$ capping," Appl. Phys. Lett., vol. 99, pp. 181102–181102-3, (2011)
40. S. Adhikary, N. Halder, S. Chakrabarti, S. Majumdar, S. Ray, M. Herrera et al., Investigation of strain in self-assembled multilayer InAs/GaAs quantum dot heterostructures. J. Cryst. Growth **312**, 724–729 (2010)

Chapter 2
Low-Energy Ion Implantation Over Single-Layer InAs/GaAs Quantum Dots

Abstract This chapter deals with the impact of both low-energy heavy ion (sulphur) and light ion (hydrogen) implantation over single-layer InAs/GaAs QDs. The material and structural properties of both un-implanted and implanted QDs are discussed, along with the results achieved through different characterizations. Sulphur (S^-) ion implantation caused degradation of material quality whereas hydrogen (H^-) ion implantation improved the material properties of InAs/GaAs QDs. The main purpose of this study was to optimize the particular ion and its energy and fluence range for experiencing the impact of ion implantation further on In(Ga)As/GaAs QD-based device structures as discussed in the following chapters.

Keywords Low-energy light ion implantation · Photoluminescence (PL) · Material properties · Blue shift of PL emissions · TRIM calculations · Ion fluence

2.1 Motivation Behind Ion Implantation Study

As mentioned in Sect. 1.6.1, in the present study, we tried to explore ion implantation as an effective post-growth method for improving QD characteristics. Our study is about the effects of ion implantation over In(Ga)As/GaAs QD heterostructures. From an application viewpoint, recent studies conducted by various research groups proved the greater radiation hardness of In(Ga)As/GaAs QD-based optoelectronic devices as compared to QW structures [1–3]. The radiation hardness in the QD structure is due to the three-dimensional quantum confinement of carriers in QDs. This unique property of QD-based devices could be

Portions of this chapter is reprinted from 1. R. Sreekumar, **A. Mandal**, **S. Chakrabarti** and S. K. Gupta, "Effect of heavy ion implantation on self assembled single layer InAs/GaAs quantum dots," ***Journal of Physics D: Applied Physics***, Vol. 43, pp. 505302, 2010, © IOP Publishing. Reproduced by permission of IOP Publishing. All rights reserved, 2. R. Sreekumar et al., "H^- ion implantation induced ten-fold increase of photoluminescence efficiency in single layer InAs/GaAs quantum dots," ***Journal of Luminescence***, vol. 153, pp. 109–117, 2014, with permission from Elsevier.

© Springer Nature Singapore Pte Ltd. 2017

A. Mandal and S. Chakrabarti, *Impact of Ion Implantation on Quantum Dot Heterostructures and Devices*, DOI 10.1007/978-981-10-4334-5_2

exploited for the fabrication of devices that are used in radiation-prone environments, such as in space crafts, satellites and nuclear power plants. The composition of high-energy galactic cosmic rays encountered in outer space is approximately 91% protons, 8% helium and 1% heavy ions having energy in the range of a few 100 MeV (mega electron volt) to 100 GeV (giga electron volt) [4]. Prior to the application of QD devices in a radiation-prone environment, one has to study the possible improvement or degradation in QD-based structures due to radiation, which would help one predict the lifetime of QD devices. For that purpose, different ion implantations must be performed over these QD heterostructures to study how the structural and material properties of these structures are modified.

When high-energy ions pass through the target material, they lose energy to the target mainly by two independent processes: (i) via elastic collision with the target nucleus and (ii) inelastic collision with the atomic electrons in the target [5, 6]. The former process results in the displacement of atoms in the target via collision cascade; this mechanism dominates when the energy transferred to the target atoms exceeds the displacement threshold. As a result, the atoms are pushed from their lattice positions and may collide with other target atoms. In this manner, a recoil cascade can be initiated where thousands of atoms are relocated by a single ion. If this process occurs in the vicinity of an interface, it can result in atomic mixing across the interface. The latter process (inelastic collision) involves the transfer of energy to the target electron as kinetic energy first, and this kinetic energy is transferred to the lattice via electron–phonon interaction. This can result in a thermal spike that is quenched in a few picoseconds, and can result in the formation of amorphous tracks in the target materials [6]. Keeping aside these effects, our main aim is to find if ion implantations help in annihilating the defects present in as-grown QD heterostructures. Removal of the defects from these heterostructures can improve QD characteristics.

2.2 Scope of the Present Study

We performed both heavy ion (S^-) and light ion (H^-) implantations on single-layer InAs/GaAs QD heterostructure so as to compare the two. Salame et al. [7] showed that by using pre-neutron implantation, one could harden electronic devices like field effect transistors against heavy ion implantation. However, this can also result in an increase in the device production cost. The effect of heavy ion implantation on In(Ga)As/GaAs QD heterostructures without any pre-neutron implantation has not been studied previously. In this study, we selected sulphur ions to be implanted over the InAs/GaAs QD heterostructures. The energy of the ions was varied from 20 to 50 keV with a fluence ranging from 2.5×10^{13} to 2×10^{15} ions/cm^2. Being the heavier ion, sulphur was expected to create more structural disorders in the material via collision cascade [5]. We employed low-temperature PL, studied the degradation of PL induced by sulphur implantation and tried to identify the defects that are responsible for the degradation.

Improvement of material quality of In(Ga)As/GaAs QDs by hydrogen implantation has already been reported by several groups. As mentioned earlier, Leon et al. demonstrated slight enhancement of low-temperature PL emission using 1.5 MeV proton (H^+) implantation on single-layer InGaAs/GaAs QDs [1, 8]. Later, Lu et al. demonstrated enhancement of PL efficiency in multilayer InAs QDs on proton implantation (50–70 keV) followed by a rapid thermal annealing [9, 10]. In this study, we report the effects of low-energy H^- ion implantation on the InAs/GaAs QDs and how the material quality of the implanted samples was improved without any further annealing treatment.

2.3 Growth of Single-Layer InAs/GaAs QDs

InAs/GaAs QDs were grown on semi-insulating GaAs (100) substrate using the Stranski–Krastanov mode at a substrate temperature of 500 °C by solid-state MBE. First, a 0.5 μm GaAs (intrinsic) buffer layer was grown at 590 °C on the epi-ready semi-insulating GaAs substrate, after desorbing the protective oxide layer. Subsequently, the temperature was brought down to 500 °C and a thin intrinsic GaAs layer of 0.1 μm was deposited. Thereafter, 2.7 ML of InAs was deposited, which formed the wetting layer and gave rise to self-assembled QDs. These QDs were further capped by an intrinsic GaAs layer of 0.1 μm thickness. To study the morphology of the dots, similar InAs quantum dots of 2.7 ML were grown (surface dots) on the top of this 0.1 μm capping layer. A schematic diagram of the epitaxially grown InAs/GaAs QD heterostructure is shown in Fig. 2.1. The rate of deposition of GaAs was kept at ∼0.72 μm/h, whereas the growth rate of InAs dots was maintained at ∼0.2 ML/s.

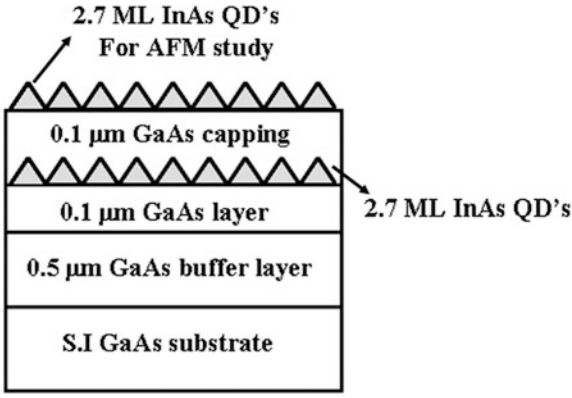

Fig. 2.1 Schematic of single-layer InAs/GaAs quantum dots (QDs) grown on semi-insulating GaAs substrate [11]

2.4 Ion Implantation and Post-Growth Experiments on QDs

A stable beam of sulphur ions (S^-) from LEAF, BARC was used for heavy ion implantation. These samples were implanted with sulphur ions of energy ranging from 20 to 50 keV at room temperature with a fluence in the range of 2.5×10^{14} ions/cm^2. The effect of sulphur ions on InAs/GaAs QDs was also studied by varying the fluence in the range of 2.5×10^{13}–2×10^{15} ions/cm^2, while maintaining the energy of the sulphur ions at 30 keV. The penetration range of 20 and 50 keV sulphur ions in InAs/GaAs system is about 201 and 407 Å, respectively, as calculated using TRIM [12]. It is to be noted that the majority of the ions are deposited in the GaAs capping layer and only a few ions managed to reach the InAs QD layer, and that too only in case of 50 keV S^- ion implantation.

For light ion implantation study, heterostructures were implanted with H^- ions at an energy of 50 keV and fluence in the range of 6×10^{12}–2.4×10^{15} ions/cm^2 using LEAF. From TRIM calculation, it was found that the penetration range of 50 keV H^- ions in InAs/GaAs system is about 0.36 µm [12].

Samples were taken out of the implantation chamber and were subjected to AFM studies in atmospheric pressure, using Veeco Digital NanoScope IV. XRD patterns were recorded in the range of $2\theta = 20°$–$100°$ using Cu K_α ($\lambda = 1.5405$ Å) radiation source by employing the PANalytical X'pert Pro system. Low-temperature and power-dependent PL measurements were performed with the PL set-up. The samples were excited with a diode-pumped solid-state laser at a wavelength of 405 nm. XTEM micrographs were recorded under an acceleration voltage of 200 kV with a Philips EM420 system.

2.5 Results and Discussion

2.5.1 Structural, Material and Optical Properties of S^- Ion-Implanted InAs/GaAs QDs

Figure 2.2 shows atomic force micrographs of as-prepared InAs/GaAs QD sample and samples implanted with 50 keV sulphur ions. Implantation resulted in modification of surface dot morphology. The density of the surface dots was reduced upon implantation (from 4.4×10^{10} to 2.3×10^{10} dots/cm^2). This is probably due to the agglomeration of surface dots induced by sulphur implantation.

Figure 2.3 shows the XRD pattern of QDs implanted with sulphur ions of different energies with fluence in range of 2.5×10^{14} ions/cm^2. Figure 2.3a is the XRD pattern of the un-implanted sample. The XRD reflections centred at $2\theta = 31.70°$ along the (200) plane and at $2\theta = 66.12°$ along the (400) plane are from the GaAs substrates [13]. The reflection at $2\theta = 59.08°$ is from InAs/GaAs QDs grown along the same plane as the GaAs substrate (400) [14]. Furthermore, the

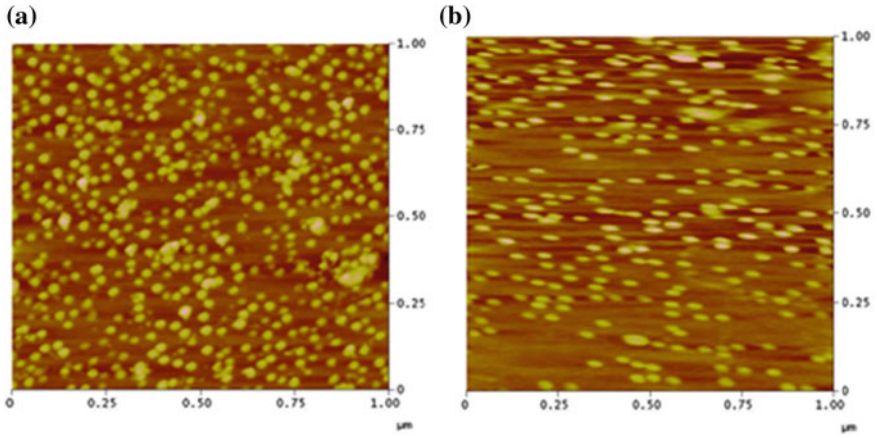

Fig. 2.2 Atomic force micrographs of InAs/GaAs quantum dots (QDs) **a** un-implanted sample, and **b** sample implanted with 50 keV sulphur ions [11]

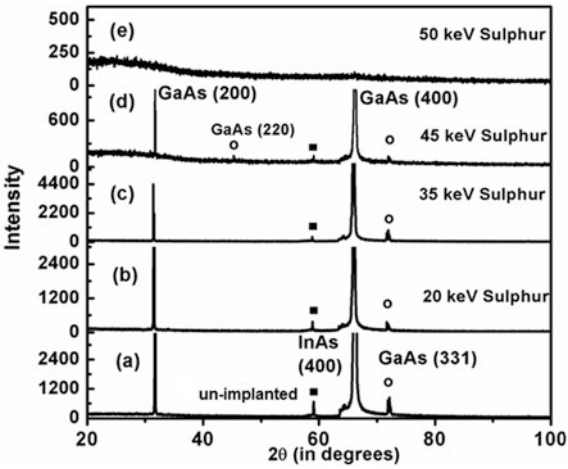

Fig. 2.3 X-ray diffraction (XRD) patterns from InAs/GaAs quantum dot (QD) heterostructures **a** un-implanted sample; samples implanted with **b** 20 keV, **c** 35 keV, **d** 45 keV and **e** 50 keV sulphur ions [11]

reflection at $2\theta = 71.88°$ along (331) is from the GaAs capping layer [15], which showed an FWHM of 0.0506°, thus exhibiting the high crystallinity of the capping layer. On implantation, the crystallinity of the GaAs capping layer degraded, as evident from the increase in FWHM of diffraction peak to 0.1162° (35 keV S^- ions). The reflection from GaAs capping layer further reduces on implanting with 45 keV S^- ions (Fig. 2.3d) and completely vanishes for 50 keV S^- ions. Interestingly, the sample also becomes completely amorphous in nature.

The amorphization of the GaAs capping layer occurred when the total nuclear energy deposited by the sulphur ions became higher than the critical energy required to create a damage zone and/or an amorphous regions in GaAs [16].

Accumulation/overlap of the initial defect clusters/displacement cascades is created during the implantation results in the amorphous zone. It was demonstrated by Wesch et al. that with a critical nuclear energy density of 8.3×10^{20} keV/cm^3, the amorphous zone could be created in GaAs [16]. Below the critical energy density, implantation creates point defects, Ga and As interstitials, vacancies, antisites and/or a complex of these defects [17]. With the increase in the nuclear energy density deposited in the system because of increasing number of ions of higher energy, the defect density also increases and saturates at critical nuclear energy density. Further increase in nuclear energy density, overlapping of defect clusters causes the transformation to the amorphous state.

Figure 2.4 shows the PL spectra recorded (at 8 K) from InAs/GaAs QDs implanted with sulphur ions of energy ranging from 20 to 50 keV. In addition, PL spectra were recorded at different laser power densities ranging from 5 to 51.6 W/cm^2 at 8 K. The ground state emission from QDs was centred at a wavelength of 1162 nm, whereas emissions from first and second excited states were at 1090 and 1026 nm, respectively.

On implantation with 20 keV S^- ions, one could notice a shift in PL emission towards lower wavelength to 1138 nm. Increase in the implantation energy resulted in a further blue shift. This observed blue shift in the PL emission could be due to two different phenomena: (a) inter diffusion of Ga into InAs QD and (b) compressive stress from the capping layer to the InAs QDs [18]. Structural damage in the GaAs capping layer enhanced the compressive stress to the InAs QDs, and thus a blue shift of the PL emission occurred [19]. Blue shift in emission wavelength due to In–Ga intermixing could be ruled out up to an implantation energy of 45 keV, since the range of the S^- ions, being bulky ions, is not long enough to reach the depths at which InAs QDs are situated. In the case of 50 keV S^- ion implantation, there is a possibility of few ions reaching the InAs QD layer at the end of its range, and giving rise to In–Ga intermixing.

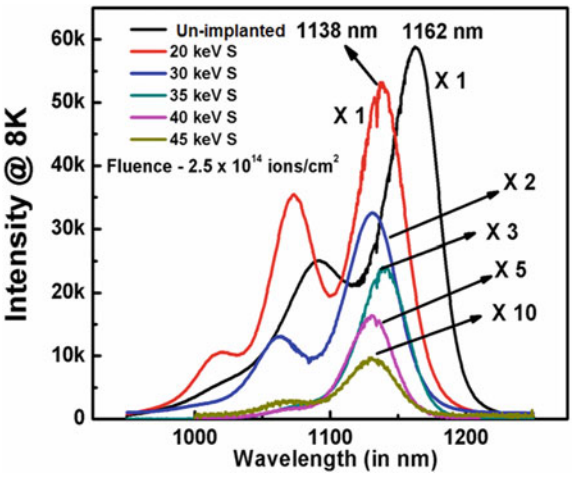

Fig. 2.4 Photoluminescence (PL) spectra at 8 K from InAs/GaAs quantum dots (QDs) implanted with sulphur ions of different energies [11]

Along with blue shift, a continuous decrease in PL intensity was observed as the energy of the sulphur ions increased from 20 to 50 keV (Fig. 2.4). For sample with implantation energy of 50 keV, luminescence degraded drastically and a broad emission peak appeared with ground state emission at 1120 nm and first excited state at 986 nm. The destruction of photogenerated carriers by non-radiative combination centres created via sulphur ion implantation can be the cause of decrease in PL intensity. With the increase in the energy of the sulphur ions, number of defects increased in the vicinity of the QDs, which resulted in increasing the rate of non-radiative transitions. As discussed earlier, below the critical nuclear energy density, sulphur ions can create point defects [17], which can also destroy the photogenerated carriers in the system and thereby degrade the PL efficiency.

Samples were further implanted with 30 keV sulphur ions of fluence ranging from 2.5×10^{13} to 2×10^{15} ions/cm^2. With increase in fluence, blue shift in PL emission along with a reduction in PL intensity was observed (Fig. 2.5). The gradual decrease in PL intensity might be due to the increase in defect density in GaAs capping layer with the increase of fluence. There was an increase in the total damage accumulated in the system, from 4.17×10^{19} to 4.17×10^{21} stable vacancies/cm^3 upon increasing the fluence ranging from 2.5×10^{13} to 2×10^{15} ions/cm^2 as per calculations done using TRIM [12].

Figure 2.6 shows how the integrated PL intensity of ground state varies with optical excitation density for both the un-implanted sample and the sample implanted with 45 keV sulphur ions. For the un-implanted sample, PL intensity increases with increase in optical excitation density. A similar trend was recorded for the samples implanted with sulphur ions up to 40 keV energy. In the un-implanted sample, lower density of non-radiative recombination centres causes saturation of these non-radiative recombination centres at lower excitation density. This saturation results in linear increase in PL intensity. However, in case of the sample implanted with 45 keV sulphur ions, the density of non-radiative recombination centres formed by structural defects is high. Naturally, PL intensity gets

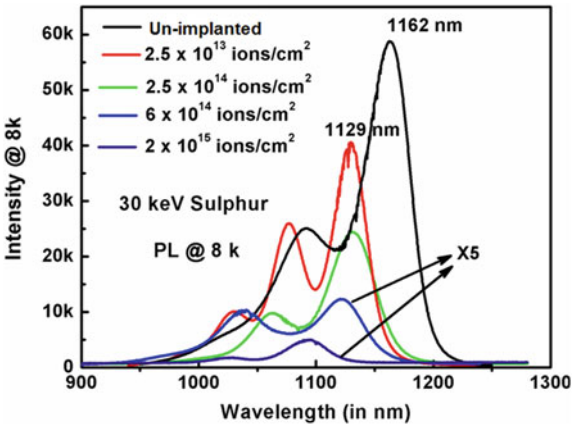

Fig. 2.5 Photoluminescence (PL) spectra at 8 K from InAs/GaAs quantum dots (QDs) implanted with 30 keV sulphur ions of different fluences [11]

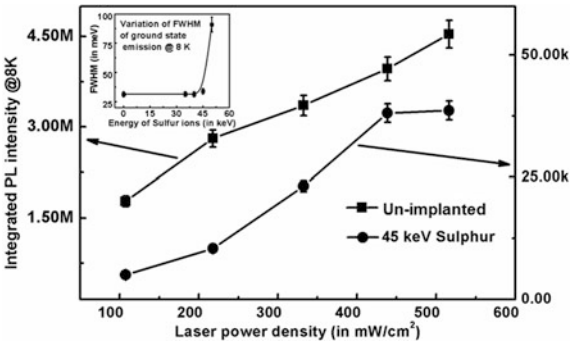

Fig. 2.6 Variation of integrated PL intensity of ground state with optical excitation density for InAs/GaAs quantum dots (QDs), both for un-implanted sample and sample implanted with 45 keV sulphur ions. Inset shows the variation of ground state PL peak FWHM with energy of sulphur ions [11]

saturated at higher excitation densities (Fig. 2.6). This proves that structural defects were formed and that in effect reduced the PL efficiency of InAs/GaAs QDs, upon sulphur implantation. A sudden increase in the ground state PL peak FWHM was observed for the sample implanted with 50 keV sulphur ions (inset of Fig. 2.6). Increase in defect density in the system can be the cause of broadening in ground state PL peak FWHM [20].

2.5.2 *Structural, Material and Optical Properties of H^- Ion-Implanted InAs/GaAs QDs*

Figure 2.7 shows the XRD patterns of the samples implanted with 50 keV H^- ions of fluences ranging from 6×10^{12} to 2.4×10^{15} ions/cm^2. XRD peaks centred at $2\theta = 66.12°$ and 31.69° along the (400) and (200) planes, respectively, are from the GaAs substrate, while that at $2\theta = 72.14°$ along the (331) plane is from the GaAs capping layer [13]. The reflection from InAs QDs along (400) plane could also be identified at $2\theta = 59.08°$.

Implantation with H^- ions at fluences in the range of 6×10^{12} and 2.4×10^{13} ions/cm^2 resulted in improvement in XRD from InAs QDs and a decrease in FWHM (Fig. 2.8). A probable reason might be the passivation of defects in the InAs/GaAs QDs created during the growth process [22]. On the other hand, XRD from the GaAs capping layer degraded as its FWHM increased. Similarly, XRD from the (222) plane of GaAs also degraded on H^- implantation (Fig. 2.7). A further increase in fluence to 7.2×10^{13} ions/cm^2 reduced the reflections from InAs QDs and GaAs capping layer. At a fluence in the range of 2.4×10^{15} ions/cm^2, the diffraction peaks from the GaAs capping layer and QDs

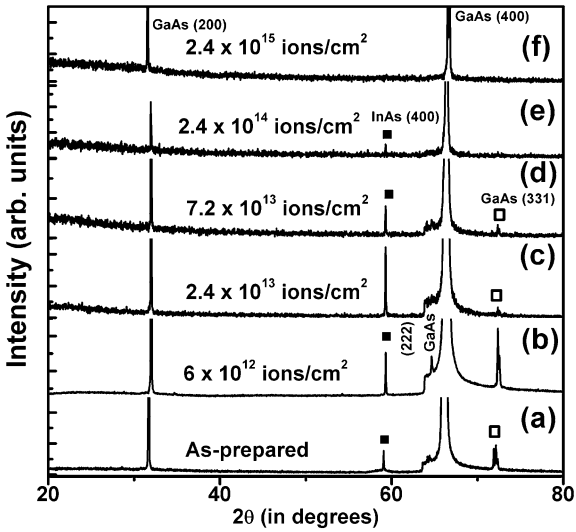

Fig. 2.7 X-ray diffraction (XRD) patterns of as-prepared sample and samples implanted with 50 keV H^- ions at different fluences [21]

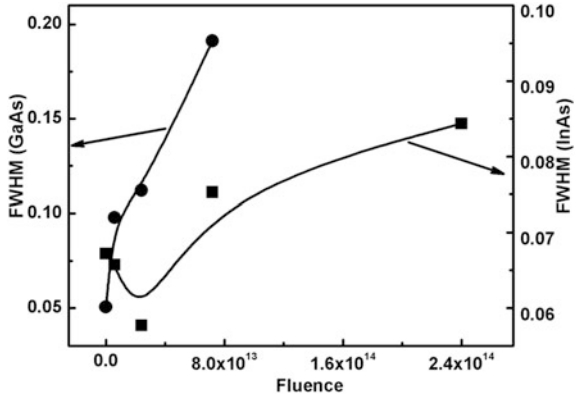

Fig. 2.8 Variation of full width at half maximum (FWHM) of X-ray reflections from InAs/GaAs quantum dots (QDs) and the GaAs capping layer with different H^- ion fluences [21]

were eliminated, indicating a reduction in the crystallinity of the heterostructure at high implantation fluence.

As the penetration range of 50 keV H^- ions in InAs/GaAs system is about $\sim$0.36 μm [12], this implantation affects surface dots as well as the embedded dots in the system. Figure 2.9 depicts the XTEM images of surface QDs recorded from the sample implanted with 50 keV H^- ions at various fluences. As the implantation fluence increases, the height of the surface QDs decreases and lateral size increases a bit relative to the as-prepared sample. This may be probably due to the intermixing taking place between the surface QDs and the GaAs capping layer interface. A similar behaviour was observed in the case of embedded dots on H^- ion implantation.

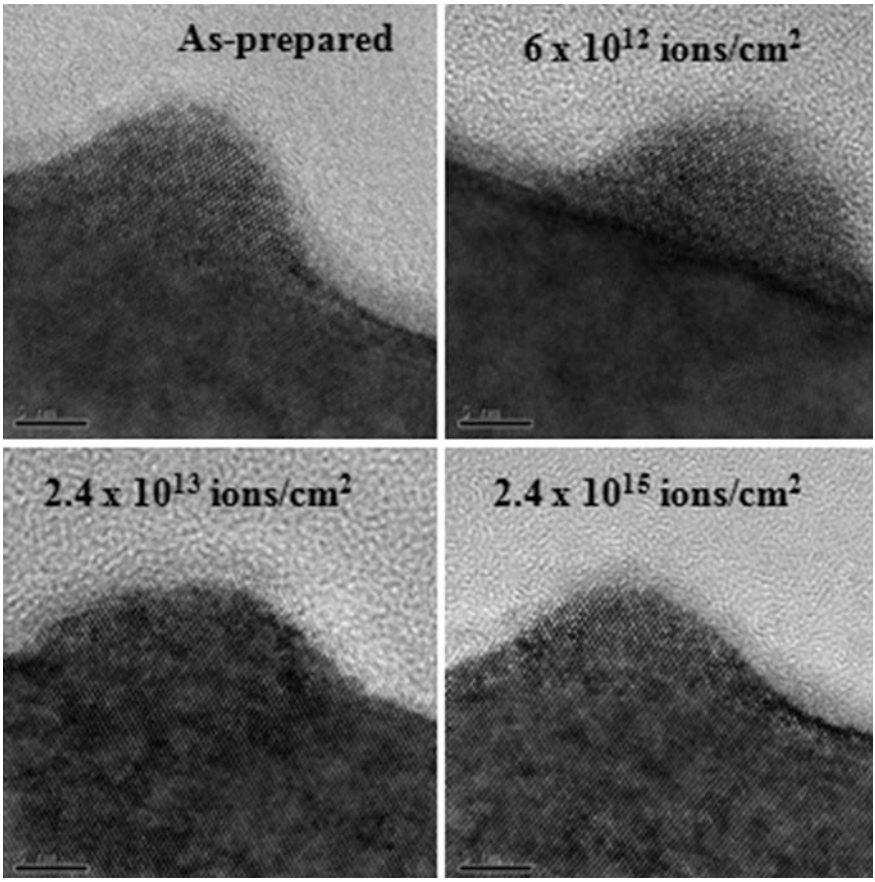

Fig. 2.9 Cross-sectional transmission electron microscopy (XTEM) images of surface dots [21]

Figure 2.10 depicts the PL spectra recorded at 8 K from the samples implanted with H^- ions of various fluences (laser excitation density ~51.6 W/cm^2). The ground sate emission from as-prepared sample was at 1160 nm. An enhancement of PL intensity was observed with H^- ion implantation up to the fluence in the range of 2.4×10^{13} ions/cm^2 and intensity decreased further. The probable reason might be the eradication of non-radiative recombination centres from the capping layer and QDs due to H^- ion implantation up to the fluence in the range of 2.4×10^{13} ions/cm^2. The same sample (implanted with fluence in the range of 2.4×10^{13} ions/cm^2) showed best crystallinity, as observed from XRD studies (Figs. 2.7 and 2.8). A blue shift in PL emission was observed with higher implantation fluence (Fig. 2.10). The XRD analysis showed that the H^- ion implantation modified the structural/crystalline property of the QDs and capping layer. The modification made by the H^- ions in the capping layer could exert compressive stress on the embedded QDs [18]. Stress induced by the capping layer

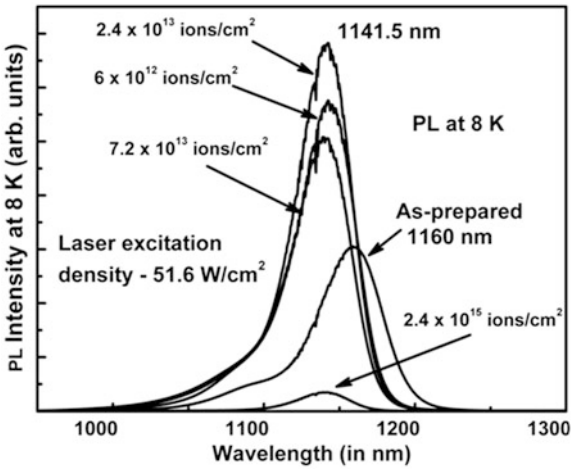

Fig. 2.10 Photoluminescence (PL) spectra recorded at 8 K with laser excitation density 51.6 W/cm^2 from samples implanted with H^- ions [21]

and the interdiffusion at the QD–capping layer interface resulted in the blue shift of the PL emission on ion implantation.

To extract information on non-radiative recombination centres, it is beneficial to record PL spectra at a low laser excitation density; i.e., a density at which the non-radiative recombination centres are more pronounced as lesser number of carriers are photogenerated in the system. A similar trend of increase in PL intensity with increasing implantation fluence was detected at 8 K (Fig. 2.11), even at a low

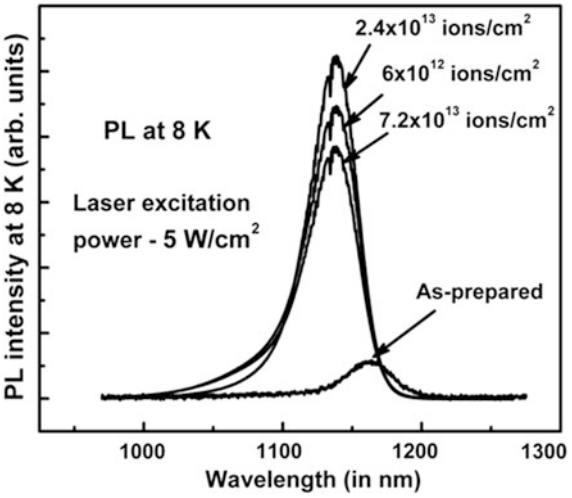

Fig. 2.11 Photoluminescence (PL) spectra recorded at 8 K with laser excitation density 5 W/cm^2 from the samples implanted with H^- ions [21]

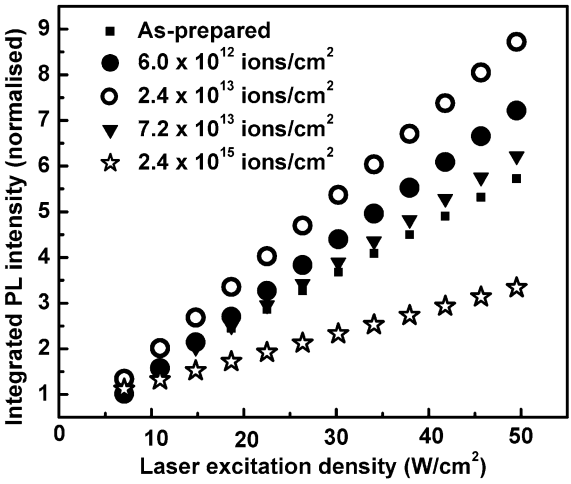

Fig. 2.12 Variation of integrated PL intensity with laser excitation density for H^- ion-implanted InAs/GaAs quantum dots (QDs) [21]

excitation density of 5 W/cm^2. The overall PL efficiency increased with fluence up to an optimum value of 2.4×10^{13} ions/cm^2. PL efficiency reduced on further increases in fluence. This experiment clearly showed that H^- ion implantation can eradicate non-radiative recombination centres in InAs/GaAs QD systems.

Figure 2.12 shows a plot of integrated PL intensity versus laser excitation density for the as-prepared and 50 keV H^- ion-implanted samples at various implantation fluence values. Each plot is normalized to its respective integrated PL intensity recorded at an excitation density of 6.5 W/cm^2. The rate of increase in integrated PL intensity with increase in excitation density was higher for the samples implanted with 6×10^{12} and 2.4×10^{13} ions/cm^2 fluence compared to the as-prepared sample (Fig. 2.12). This revealed that non-radiative recombination was reduced on H^- ion implantation owing to the increase in PL emission, as more carriers could participate in radiative recombination. On increasing the fluence to 7.2×10^{13} ions/cm^2, the rate of increase in PL intensity is reduced, reaching a value comparable to that of the as-prepared sample. With an implantation fluence in the range of 2.4×10^{15} ions/cm^2, the rate of increase in PL intensity was markedly suppressed due to the introduction of structural damage caused by high implantation dosage.

2.6 Conclusions Obtained from the Results of Heavy and Light Ion Implantation on InAs/GaAs QDs

The implantation hardness of InAs/GaAs QDs was tested in the critical energy density regime (to create an amorphous zone) with S^- ions of fluence in the range of 2.5×10^{14} ions/cm^2. Sulphur implantation created structural defects/lattice damage

in the GaAs capping layer, which resulted in the destruction of photogenerated carriers by non-radiative recombination and thereby degrading the PL efficiency. The damaged capping layer induced compressive stress in the InAs dots, which changed the energy gap of the dots and caused a blue shift in the emission wavelength. The study of fluence dependence revealed that on sulphur ion implantation, the PL efficiency decreases with increase in total damage accumulated in the capping layer.

With light ion (H^-) implantation, we demonstrated the enhancement of PL efficiency in single-layer InAs/GaAs QD heterostructures without the need for any annealing treatment. The optimum fluence at which maximum PL efficiency was attained using 50 keV H^- ions was 2.4×10^{13} ions/cm^2. The introduction of structural damage on increasing the fluence beyond an optimum value resulted in the degradation of the PL efficiency. The increase in PL efficiency is attributed to the eradication of non-radiative recombination centres present at the GaAs capping layer–QD interface, the wetting layer and in the QDs.

We can thus summarize that heavy ion implantation results in degradation of the material quality of InAs/GaAs QD heterostructures and that heavy ion implantation is not further suitable for the present study. Conversely, we found that light ions (H^-) are ideal for further experiments on implantation over In(Ga)As/GaAs QD heterostructures to establish ion implantation as an effective post-growth method in improving material quality as well as device performance.

References

1. R. Leon, G. Swift, B. Magness, W. Taylor, Y. Tang, K. Wang et al., Changes in luminescence emission induced by proton irradiation: InGaAs/GaAs quantum wells and quantum dots. Appl. Phys. Lett. **76**, 2074–2076 (2000)
2. P. Piva, R. Goldberg, I. Mitchell, D. Labrie, R. Leon, S. Charbonneau et al., Enhanced degradation resistance of quantum dot lasers to radiation damage. Appl. Phys. Lett. **77**, 624–626 (2000)
3. C. Ribbat, R. Sellin, M. Grundmann, D. Bimberg, N. Sobolev, M. Carmo, Enhanced radiation hardness of quantum dot lasers to high energy proton irradiation. Electron. Lett. **37**, 174–175 (2001)
4. D. Rapp, MARS. Mars **2**, 72–82 (2006)
5. W. Bolse, Atomic transport in thin film systems under heavy ion bombardment. Surf. Coat. Technol. **158**, 1–7 (2002)
6. G. Schiwietz, E. Luderer, G. Xiao, P. Grande, Energy dissipation of fast heavy ions in matter. Nucl. Instrum. Methods Phys. Res., Sect. B **175**, 1–11 (2001)
7. C. Salame, A. Hoffmann, F. Pelanchon, P. Mialhe, J. Charles, Effects of the pre-neutron irradiation on VDMOSFET sensitivity to heavy ions. Microelectron. Int. **18**, 16–20 (2001)
8. R. Leon, S. Marcinkecius, J. Siegert, B. Cechavicius, B. Magness, W. Taylor et al., Effects of proton irradiation on luminescence emission and carrier dynamics of self-assembled III–V quantum dots. Nucl. Sci. IEEE Trans. **49**, 2844–2851 (2002)
9. W. Lu, Y. Ji, G. Chen, N. Tang, X. Chen, S. Shen et al., Enhancement of room-temperature photoluminescence in InAs quantum dots. Appl. Phys. Lett. **83**, 4300–4302 (2003)

10. Y. Ji, G. Chen, N. Tang, Q. Wang, X. Wang, J. Shao et al., Proton-implantation-induced photoluminescence enhancement in self-assembled InAs/GaAs quantum dots. Appl. Phys. Lett. **82**, 2802–2804 (2003)
11. R. Sreekumar, A. Mandal, S. Chakrabarti, S.K. Gupta, Effect of heavy ion implantation on self assembled single layer InAs/GaAs quantum dots. J. Phys. D Appl. Phys. **43**, 505302 (2010)
12. J.F. Ziegler, J.P. Biersack, U. Littmark, PC programme package TRIM95, 1995
13. International Centre for Diffraction Data: Powder Diffraction File: 80-0016
14. International Centre for Diffraction Data: Powder Diffraction File: 15-0869
15. International Centre for Diffraction Data: Powder Diffraction File: 80-0003
16. W. Wesch, E. Wendler, G. Gotz, N. Kekelidse, Defect production during ion implantation of various $A_{III}B_V$ semiconductors. J. Appl. Phys. **65**, 519–526 (1989)
17. A.G. Milnes, *Advances in Electronics and Electron Physics* (Academic Press, New York, 1983, pp. 64–161)
18. H. Saito, K. Nishi, S. Sugou, Influence of GaAs capping on the optical properties of InGaAs/GaAs surface quantum dots with 1.5 μm emission. Appl. Phys. Lett. **73**, 2742–2744 (1998)
19. Z. Niu, X. Wang, Z. Miao, S. Feng, Modification of emission wavelength of self-assembled In(Ga)As/GaAs quantum dots covered by $In_xGa_{1-x}As$ ($0 \leqslant x \leqslant 0.3$) layer. J. Cryst. Growth **227**, 1062–1068 (2001)
20. V. Babentsov, F. Sizov, Defects in quantum dots of IIB–VI semiconductors. Opto-Electron. Rev. **16**, 208–225 (2008)
21. R. Sreekumar, A. Mandal, S. Chakrabarti, S.K. Gupta, H^- ion implantation induced ten-fold increase of photoluminescence efficiency in single layer InAs/GaAs quantum dots. J. Lumin. **153**, 109–117 (2014)
22. M. Gal, A. Tavendale, M. Johnson, B. Usher, Passivation of interface defects in lattice-mismatched InGaAs/GaAs heterostructures with hydrogen. J. Appl. Phys. **66**, 968–970 (1989)

Chapter 3
Optimizations for Quaternary Alloy (InAlGaAs)-Capped InAs/GaAs Multilayer Quantum Dots

Abstract As discussed in the last chapter the effects of both light and heavy ion implantations on InAs/GaAs QDs for the ion optimization purpose, it is also necessary to select ideal In(Ga)As/GaAs QD-based heterostructures to navigate the effects of ion implantations on them, i.e. we must go for heterostructures which can produce devices with high efficiency. In this chapter, the structural and optoelectronic properties of quaternary alloy (InAlGaAs)-capped multilayer In(Ga)As/GaAs QD heterostructures were investigated by varying growth rate, capping layer thickness and seed QD monolayer coverage. We had already discussed in the first chapter the effects of capping layers over InAs QDs. In addition, when all the samples were annealed at various temperatures, the results showed that structural and optoelectronic properties are greatly influenced by annealing temperatures.

Keywords Multilayer QDs · Quaternary alloy (InAlGaAs) capping · Seed monolayer coverage · Rapid thermal annealing (RTA) · Intermediate-band-gap solar cells · Multimodal QDs

Portions of this chapter is reprinted from 1. **A. Mandal** et al., "Thermal stability of quaternary alloy (InAlGaAs)-capped InAs/GaAs multilayer quantum dot heterostructures with variation in growth rate, barrier thickness, seed quantum dot monolayer coverage, and post-growth annealing", ***Applied Physics A Materials Science & Processing*** (DOI 10.1007/s00339-012-7521-2), 2. **A. Mandal** et al., "The impact of monolayer coverage, barrier thickness and growth rate on the thermal stability of photoluminescence of coupled InAs/GaAs quantum dot hetero-structure with quaternary capping of InAlGaAs" ***Materials Research Bulletin***, Vol. 47, pp. 551–556, 2012, 3. **A. Mandal** et al., "Effects of ex situ annealing on quaternary alloy (InAlGaAs) capped InAs/GaAs quantum dot heterostructures on optimization of optoelectronic and structural properties with variation in growth rate, barrier thickness, and seed quantum dot monolayer coverage," ***Superlattices and Microstructures***, Vol. 58, pp. 101–119, 2013, with permission from Elsevier.

© Springer Nature Singapore Pte Ltd. 2017

A. Mandal and S. Chakrabarti, *Impact of Ion Implantation on Quantum Dot Heterostructures and Devices*, DOI 10.1007/978-981-10-4334-5_3

3.1 Motivation Behind the Study

After we established in previous chapter that low energy light ion implantation could enhance the material properties of single-layer InAs/GaAs QDs, our immediate focus was to validate these improvements in case of In(Ga)As/GaAs QD-based device structures, i.e. to check whether low energy light ion implantation could improve device performance. Another significant aspect of our study, as mentioned earlier, was to introduce quaternary alloy (InAlGaAs) capping over the dots to improve QD characteristics. We studied quaternary alloy-capped InAs/GaAs multilayer quantum dots (MQDs) in this chapter from both these viewpoints. Multilayer QD structures are used as active regions in the QD-based devices. In this study, the structural and optoelectronic properties of coupled MQD heterostructures were investigated by varying the growth rate, capping layer thickness and seed QD monolayer coverage. In addition, post-growth rapid thermal annealing was performed on all the samples, and the results showed that structural and optoelectronic properties were greatly influenced by annealing temperatures. Our main aim was to optimize the properties of these MQD heterostructures for their suitable device applications.

3.2 Importance of Multilayer QDs

To date, many studies had been conducted on various properties of single-layer [1, 2], bi-layer [3, 4] and multilayer QDs (MQDs) [5–9]. A specific goal of using MQDs is to achieve greater active volume compared to single- or bi-layer QDs [10], a feature that can be beneficial in enhancing QD properties such as modal gain and optical sensitivity [5, 10, 11]. Such properties have been investigated for optimizing the characteristics of coupled MQDs for their efficient employment in devices such as photodetectors [12–14], lasers [15–17] and intermediate-band-gap solar cells [18, 19]. Due to the presence of a larger active region attributed to a greater number of effective dot layers in MQDs, the modal gain of lasers increases [15–17, 20]. Compared to single-layer QDs, electronically coupled MQDs have enhanced capture efficiency and localization energy, which are helpful in applications like photodetectors [12–14]. The presence of inhomogeneous strain and the overall strain in a QD system leads to multilayer stacking, which in turn helps in the formation of intermediate energy bands and is beneficial in producing highly efficient intermediate-band-gap solar cells [18, 19].

3.3 Growth of Different Quaternary Alloy-Capped Multilayer InAs/GaAs QDs

Ten-layered InAs/GaAs MQD samples were grown over a semi-insulating (100) GaAs substrate using solid source MBE and the Stranski–Krastanov growth technique. A schematic representation of the heterostructure (Fig. 3.1) and a

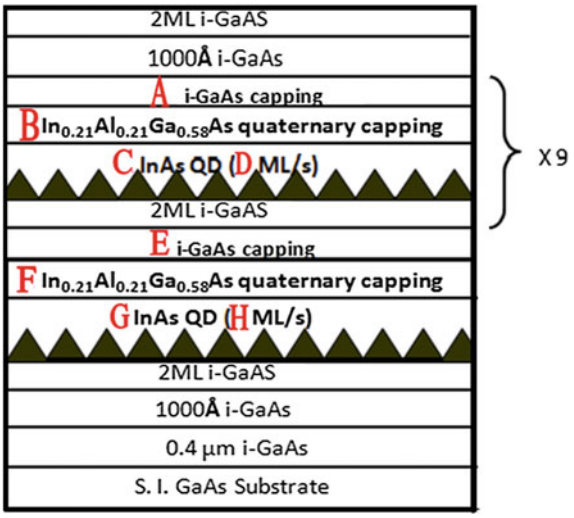

Fig. 3.1 Heterostructure of the multilayer quantum dot (MQD) sample as specified in Table 3.1 [21]

table showing the specifications (Table 3.1) completely describe the structure of each sample. First, an intrinsic 0.4-µm-thick GaAs buffer layer was grown at 600 °C on the GaAs substrate, followed by the growth of the 1000 Å intrinsic GaAs layer at 520 °C. The seed layer of InAs QD for each structure was grown at 520 °C and capped with a combination of a quaternary $In_{0.21}Al_{0.21}Ga_{0.58}As$ layer and an intrinsic GaAs layer according to the specifications given in Table 3.1. The remaining nine layers of active QDs for all the samples were grown at 480 °C to avoid In/Ga intermixing [16] with the capping combinations shown in Table 3.1. All samples were grown at the rates specified in Table 3.1.

Table 3.1 Specifications of basic heterostructure of various InAlGaAs-capped multilayer InAs/GaAs quantum dot (QD) heterostructures

Sample name	A (Å)	B (Å)	C (ML)	D (ML/s)	E (Å)	F (Å)	G (ML)	H (ML/s)
A1	90	30	2.7	0.2011	90	30	2.7	0.2011
A2	90	30	2.7	0.09411	90	30	2.7	0.09411
B1	80	20	2.5	0.2011	80	20	2.5	0.2011
B2	130	20	2.5	0.2011	90	20	2.7	0.2011
B3	130	20	2.5	0.2011	90	20	2.5	0.2011

Heading symbols: *A* capping layer thickness of GaAs capping in active region; *B* capping layer thickness of quaternary InAlGaAs capping in active region; *C* thickness of InAs QD layer in active region; *D* growth rate of InAs QD layer in active region; *E* capping layer thickness of GaAs capping over seed QD layer; *F* capping layer thickness of quaternary InAlGaAs capping over seed layer; *G* thickness of InAs seed QD layer; and *H* growth rate of InAs seed QD layer [21]

3.4 Post-Growth Experiments Performed on MQDs

Post-growth annealing was performed for all samples. Each sample was subjected to rapid thermal annealing (AS ONE 150, Annealsys) for 30 s at 650, 700, 750 and 800 °C with a GaAs proximity capping. XTEM micrographs were recorded for both as-grown and annealed samples under an acceleration voltage of 200 kV with the Philips EM420 system. Temperature-dependent PL and power-dependent PL were used to examine all the samples. The samples were excited with a diode-pumped solid-state laser at a wavelength of 532 nm.

3.5 Results and Discussion

Vertically stacked QD columns were detected in all samples, as shown in the TEM images in Fig. 3.2. All vertical stacks can be seen propagating through multiple layers in the strain-contrast TEM images. This trend of vertical stacking supports

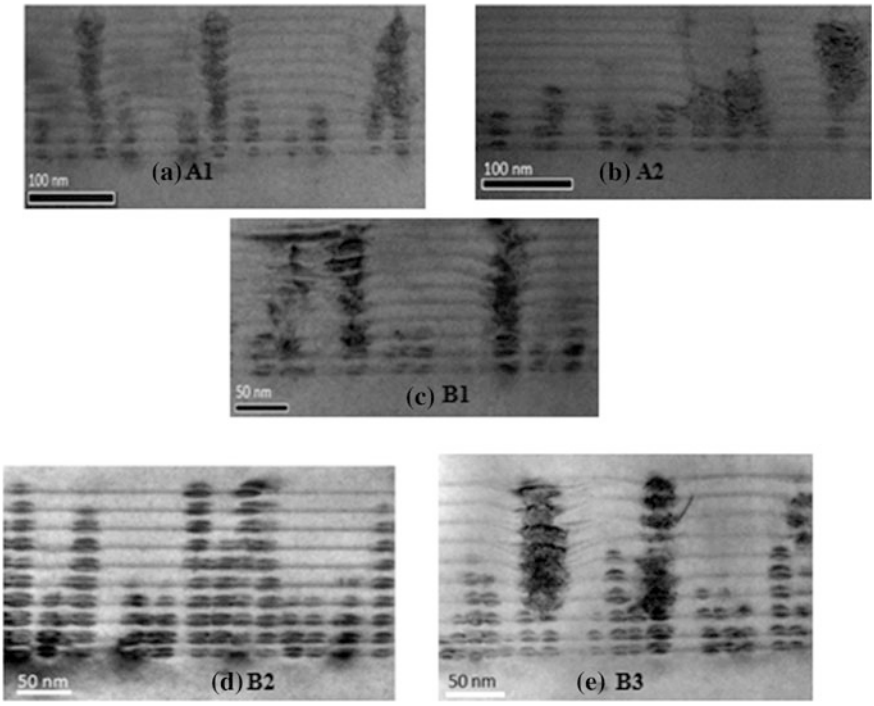

Fig. 3.2 Transmission electron microscopy (TEM) images of **a** sample A1, **b** sample A2, **c** sample B1, **d** sample B2 and **e** sample B3 [21]

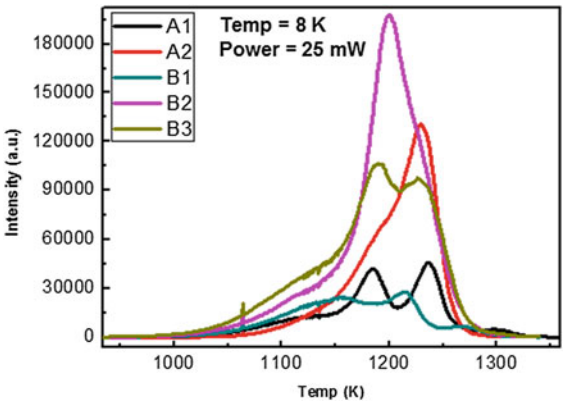

Fig. 3.3 Comparison of low-temperature photoluminescence (PL) of all as-grown multilayer quantum dot (MQD) samples giving an approximation of their emission peaks [21]

the presence of an inhomogeneous strain that is restricted to each individual layer of the QD islands [5].

All samples showed prominent PL peaks at 8 K when recorded with a laser excitation power of 25 mW (Fig. 3.3). PL emission from all the samples was between 1.1 and 1.3 μm, a technologically significant emission range that is useful for intermediate-band solar cells and communication lasers.

3.5.1 Effects of Variation in Growth Rate of QDs in InAs/GaAs MQD System

To study the effect of growth rate variation on the structural and optoelectronic properties of the MQD heterostructures, we compared the results from samples A1 and A2 while keeping other parameters such as capping layer thickness and monolayer coverage constant. Spectrally broad luminescence from these samples is a result of QD height and diameter fluctuation in the multiple layers, and consequently, the DOS is distributed over a wide energy range [22]. The peak at 1064 nm in the plots is related to the excitation laser's wavelength. The power-dependent PL results for the as-grown sample A1 are shown in Fig. 3.4, where all peaks were present even at the lowest power. Further, the plots show that even with increase in power, the relative increase in intensity for all the peaks maintained an almost constant ratio. These observations indicate that these peaks correspond to the ground states of the different dot families, thus making sample A1 multimodal [23].

Similarly, the power-dependent PL plot of the as-grown sample A2 (Fig. 3.5) showed that sample A2 had three peaks. Two of these peaks correspond to the ground state peaks of the different QD families, thus making it nearly bimodal. However, the PL peak at the shortest wavelength was absent at low excitation power, suggesting that it was an emission corresponding to the first excited state of

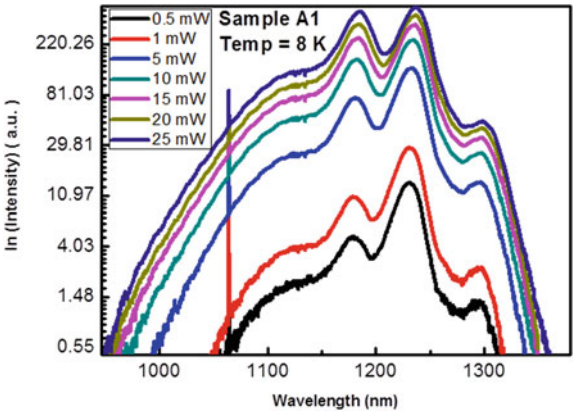

Fig. 3.4 Excitation-power-dependent photoluminescence (PL) plot of sample A1 demonstrating number of quantum dot (QD) families [21]

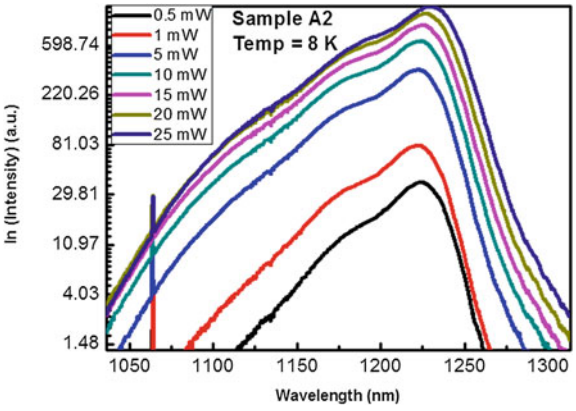

Fig. 3.5 Excitation-power-dependent photoluminescence (PL) results of sample A2 demonstrating number of quantum dot (QD) families [21]

a dot family. This observation could only be explained by the growth rate of A1 being substantially higher than that of A2. Thus, during growth, the constituent material probably preferred moving to new nucleation sites rather than moving to sites in which nucleation had already started, thereby increasing dot density and in turn reducing dot size [11]. The slower growth rate of sample A2 provided enough time for the material to be deposited at sites where nucleation had already begun, thereby creating dots of a relatively larger size; however, dot density decreased and hence fewer dot families were present. Being multimodal, both the MQD samples are beneficial in the application of intermediate-band-gap solar cells.

3.5.2 Impact of Variation in Quaternary Capping Thickness in InAs/GaAs MQD System

To analyse the effects of capping layer thickness in the MQD heterostructures, we compared samples B1, B2 and B3 (Table 3.1). The thick combination-capping layer (20 Å InAlGaAs + 130 Å GaAs) of samples B2 and B3 helps with strain compensation [5] and in the formation of high-quality dots. As discussed above, the presence of a thick GaAs barrier layer in these two samples provided the necessary Ga adatoms to fill the surface distortions of the quaternary alloy (due to strain-driven phase separation) and provide a smooth surface for the growth of subsequent dot layers. Compared to B1, which had a capping combination of 20 Å InAlGaAs + 80 Å GaAs, samples B2 and B3 had high-quality dots vertically stacked up to the top layers (Fig. 3.2). Due to the thin GaAs overgrowth in sample B1, extensive strain was developed and this in turn supported the formation of defects and threading dislocations in the heterostructure [5]. These defects and threading dislocations acted as sinks for the In atoms during MBE growth. Therefore, the supply of In atoms in the upper layers during the growth phase became insufficient and dot formation was quenched [23, 24]. This result can be observed from the TEM image of sample B1 (Fig. 3.2c), in which there was no QD formation in the top 4–5 layers of the stacks.

3.5.3 Effects of Variations in Seed QD Monolayer Coverage for Quaternary Alloy-Capped InAs/GaAs MQDs

To analyse the effects of monolayer coverage of the seed layer in the MQD heterostructure, we compared samples B1, B2 and B3 (Table 3.1). Samples B1 and B3 were grown with lower monolayer coverage of the seed QD layer (2.5 ML) than sample B2 (2.7 ML). This approach made the samples useful for comparing the extent of the seed layer effect, which initiates non-localized strain in the sample and facilitates vertical stacking of QDs through multiple layers.

Due to the greater monolayer coverage of sample B2 (Table 3.1), the seed QD layer had increased inhomogeneous strain, which led to good propagation of the vertical QD stacks through the multiple layers. This phenomenon occurs because the lattice-mismatched strain in a QD decreases with the vertical distance from the base, and the QDs with greater monolayer coverage have more relaxed lattices in the periphery. Moreover, the diffusion of In atoms from the quaternary alloy into the vicinity of the QDs increases during quaternary capping growth due to increased non-localized surface strain (inhomogeneous strain) and strain-driven phase separation. Thus, there was a greater aggregation of In atoms near the elastically relaxed regions of the islands in B2. Vertical stacking of the dots was favoured by this phenomenon, as supported by the TEM results (Fig. 3.2). The increased stacking

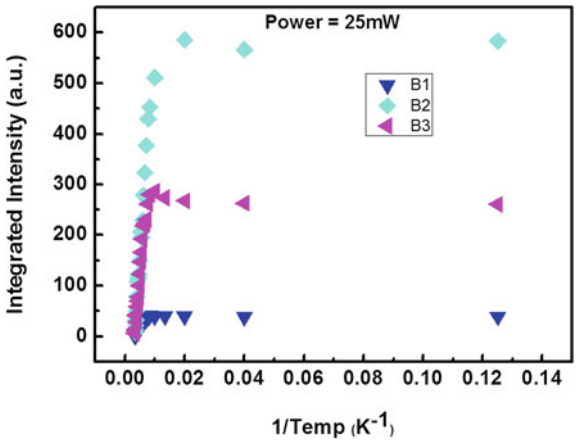

Fig. 3.6 Temperature-dependent integrated photoluminescence (PL) intensity plot of as-grown samples B1, B2 and B3 [21]

also led to higher radiative recombination due to the formation of good-quality coupled dots in the successive layers, as observed from the PL (Fig. 3.3) and integrated PL (Fig. 3.6) plots.

3.5.4 Effects of Rapid Thermal Annealing (Ex-Situ) on Quaternary Alloy-Capped InAs/GaAs MQDs

On analysing the PL plots of the annealed samples, we observed that for sample A1, there was little shift in the peak positions on annealing up to 700 °C (Fig. 3.7), whereas in sample A2, there was a consistent blue shift with annealing (Fig. 3.8). This phenomenon occurred because A2 had a much slower growth rate than A1. This slower growth rate led to the formation of large QDs. When sample A2 was annealed, the constituent materials of the larger QDs started diffusing out, and hence, the overall size of the QD decreased. The apparent diffusion led to a PL blue shift.

A similar phenomenon of In–Al intermixing occurring simultaneously has been reported [24]. The presence of Al actually increases the phase separation mechanism because of the bond energy differences between the In–As and Al–As bonds. The Al atoms from the quaternary alloy replace the In atoms from the wetting layer. During the growth phase, these In atoms diffuse into the QDs and increase QD size, which in turn leads to a red shift that counterbalances the blue shift effect [5]. Thus, overall, the peaks maintain a constant position despite undergoing annealing. At higher temperatures (750 °C and above), some degree of blue shift is seen because the mobility of the Ga adatoms increases at those high temperatures [24] and because the QDs diffuse into the wetting layer [25]; both phenomena support the

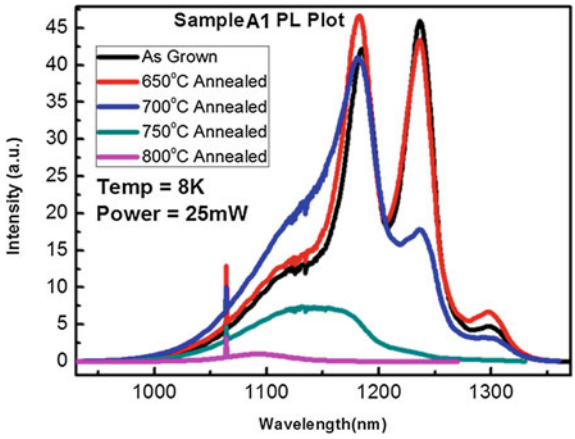

Fig. 3.7 Photoluminescence (PL) spectra depicting the thermal stability of sample A1 for different annealing temperatures [21]

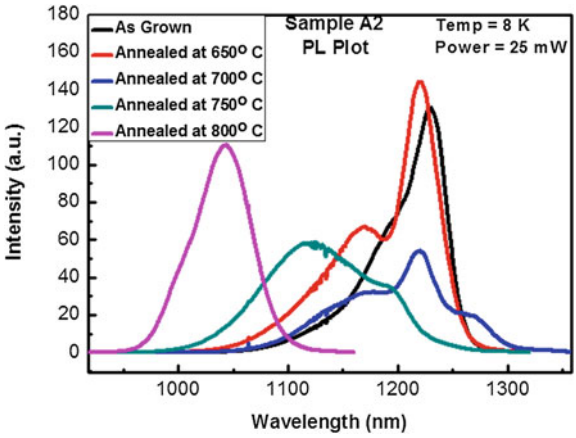

Fig. 3.8 Photoluminescence (PL) spectra depicting thermal stability of sample A2 for different annealing temperatures [21]

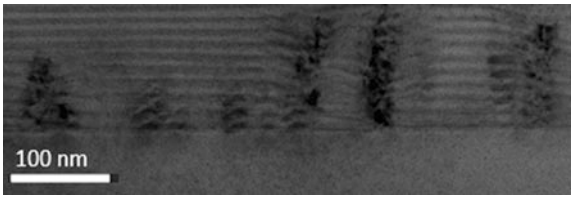

Fig. 3.9 Transmission electron microscopy (TEM) image of sample A2 annealed at 800 °C, depicting the degradation of quantum dots (QDs) at high temperatures [21]

conclusion that In–Ga interdiffusion results in a blue shift. This conclusion is supported by the TEM images of sample A2 annealed at 800 °C (Fig. 3.9) in which no distinct QDs can be observed as most had been disintegrated.

On annealing, sample A2 exhibited a drastic change in its properties. As mentioned earlier, the as-grown sample A2 had only two dot families. Annealing at 650 °C did not affect the dot density; however, annealing at 700 °C increased the

number of dot families to three. We concluded this result based on our interpretation of the power-dependent PL plots of sample A2 annealed at 650 °C (Fig. 3.10a) and 700 °C (Fig. 3.10b). Figure 3.10a shows only two peaks corresponding to the ground states of the dot families, which is the same as the number of dot families present in the as-grown sample A2. However, Fig. 3.10b shows three distinct peaks in the PL plot, which are present even at the minimum laser excitation power, signifying the presence of ground states for three distinct QD families. This suggests that the number of dot families increased after annealing at 700 °C. As explained earlier, because of the slow growth rate, the large dots were formed and dot density was low [18] in sample A2. When annealed at 700 °C, because of the high annealing temperature, the constituent material from the periphery of the larger dots started to diffuse into the smaller dots [25]. This action

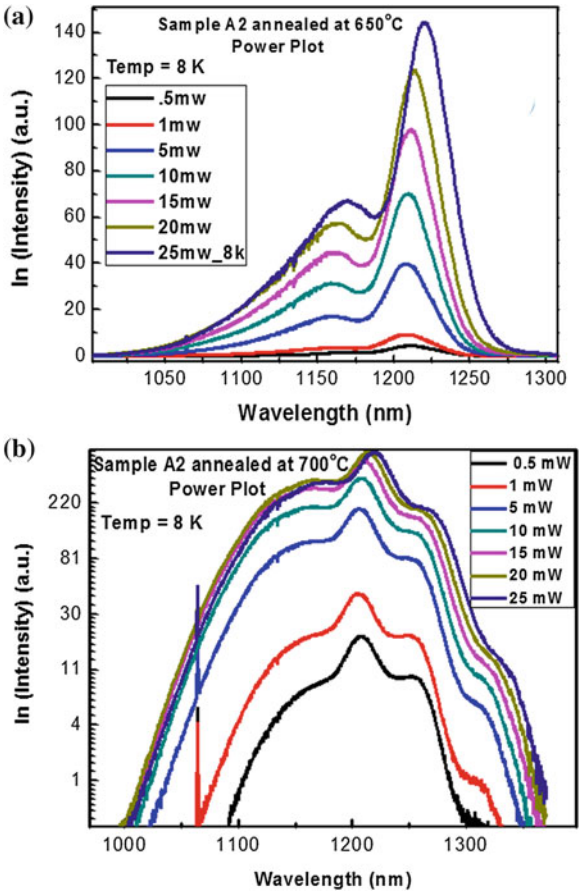

Fig. 3.10 Power-dependent photoluminescence (PL) spectra of sample A2 **a** annealed at 650 °C, depicting two quantum dot (QD) families, and **b** annealed at 700 °C, depicting three quantum dot families [21]

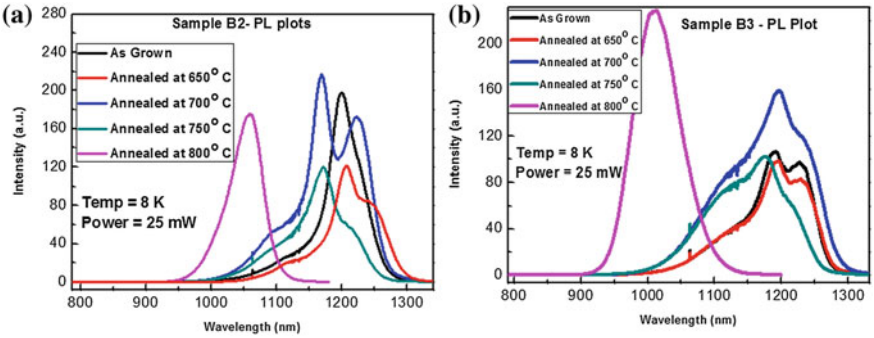

Fig. 3.11 Low-temperature photoluminescence (PL) spectra for annealed **a** sample B2 and **b** sample B3 [21]

would lead to a redistribution of the constituent material and an increase in the number of dot families. The variation in the number of dot families at different annealing temperatures highlights how annealing can be used to modify QD properties and characteristics beneficially.

The low-temperature PL plots of samples B2 and B3 annealed at various temperatures (Fig. 3.11a, b) show that these samples were thermally stable with respect to PL peak positions.

The peak positions of B2 and B3 showed negligible blue shifts with annealing temperatures up to 750 °C compared to the blue shift in sample B1 (Fig. 3.12), and these two samples had better stability than sample A1, which was thermally stable only up to 700 °C. These better results for samples B2 and B3 can be attributed to the greater capping layer thicknesses compared to those in samples B1 and A1 (Table 3.1).

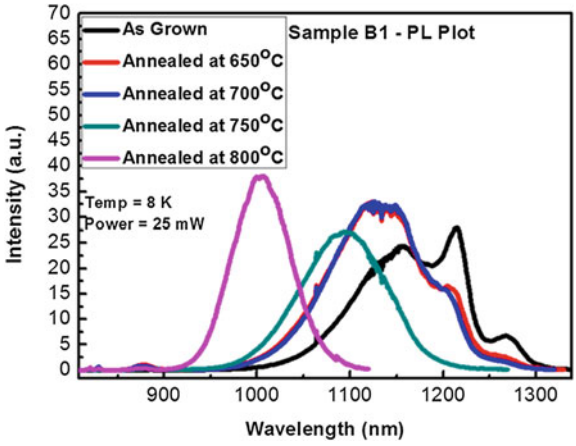

Fig. 3.12 Low-temperature photoluminescence (PL) spectra for annealed sample B1 [21]

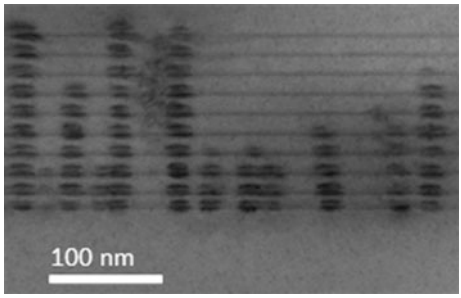

Fig. 3.13 Transmission electron microscopy (TEM) image of sample B2 annealed at 750 °C [21]

As mentioned earlier, greater capping layer thickness led to the formation of vertically stacked QDs of good quality up to the top layers. Moreover, the In atom concentration gradient along the periphery of the dots must be greater in samples B2 and B3, which prevents In atom out-diffusion and In–Ga interdiffusion, thus contributing to the thermal stability of these samples. All these results regarding the thermal stability of samples B2 and B3 are supported by TEM images. Figure 3.13 shows the TEM image of sample B2 annealed at 750 °C where the QDs are well stacked up to the top layers, as they were in the as-grown sample (Fig. 3.2d). This encouraged us to explore devices with greater capping layer thicknesses.

3.6 Significant Results of Study of Quaternary Alloy-Capped InAs/GaAs MQDs

Because of their multimodal nature, all the samples can have intermediate bands of energy, making them optimal for use in intermediate-band-gap solar cells. Sample B2 highlights the importance of greater monolayer coverage of the seed QD layer. Moreover, a thicker combination of capping layers used in samples B2 and B3 resulted in a better formation of dots in various layers and better thermal stability. Our study also shows the importance of annealing when optimizing the optoelectronic and structural properties of MQD heterostructures. Sample A2, grown at a slower growth rate, had fewer QD families in the as-grown sample, but the number of QD families increased with annealing at 700 °C. This particular result is fascinating as it offers a technique to allow some control over the number of QD families and their post-growth manipulation, thereby addressing one of the prime research concerns in this field. Further, the samples are thermally stable with an increase in modal gain due to larger active regions, a characteristic that is suitable for communication lasers.

References

1. J.-Y. Marzin, J.-M. Gérard, A. Izrael, D. Barrier, G. Bastard, Photoluminescence of single InAs quantum dots obtained by self-organized growth on GaAs. Phys. Rev. Lett. **73**, 716–719 (1994)
2. N. Kirstaedter, O. Schmidt, N. Ledentsov, D. Bimberg, V. Ustinov, A.Y. Egorov et al., Gain and differential gain of single layer InAs/GaAs quantum dot injection lasers. Appl. Phys. Lett. **69**, 1226–1228 (1996)
3. P. Siverns, S. Malik, G. McPherson, D. Childs, C. Roberts, R. Murray et al., Scanning transmission-electron microscopy study of InAs/GaAs quantum dots. Phys. Rev. B **58**, R10127–R10130 (1998)
4. Y.I. Mazur, Z.M. Wang, G. Tarasov, M. Xiao, G. Salamo, J. Tomm, et al., Interdot carrier transfer in asymmetric bilayer InAs/GaAs quantum dot structures. Appl. Phys. Lett. **86**, 063102–063102-3 (2005)
5. J. Tatebayashi, N. Nuntawong, P.-S. Wong, Y. Xin, L. Lester, D. Huffaker, Strain compensation technique in self-assembled InAs/GaAs quantum dots for applications to photonic devices. J. Phys. D: Applied Physics **42**, 073002 (2009)
6. N. Nuntawong, S. Birudavolu, C. Hains, S. Huang, H. Xu, D. Huffaker, Effect of strain-compensation in stacked 1.3 μm InAs/GaAs quantum dot active regions grown by metalorganic chemical vapor deposition. Appl. Phys. Lett. **85**, 3050–3052 (2004)
7. G. Solomon, J. Trezza, A. Marshall, J.S. Harris, Vertically aligned and electronically coupled growth induced InAs islands in GaAs. Phys. Rev. Lett. **76**, 952–955 (1996)
8. P. Joyce, T. Krzyzewski, G. Bell, B. Joyce, T. Jones, Composition of InAs quantum dots on GaAs (001): direct evidence for (In, Ga) As alloying. Phys. Rev. B **58**, R15981–R15984 (1998)
9. K. Yamaguchi, K. Yujobo, T. Kaizu, Stranski–Krastanov growth of InAs quantum dots with narrow size distribution. Japan. J. Appl. Phys. **39**, 1245 (2000)
10. H. Liu, I. Sellers, M. Gutierrez, K. Groom, W. Soong, M. Hopkinson et al., Influences of the spacer layer growth temperature on multilayer InAs/GaAs quantum dot structures. J. Appl. Phys. **96**, 1988–1992 (2004)
11. C. Chia, Y. Zhang, S. Wong, S. Chua, A. Yong, S. Chow, Testing the upper limit of InAs/GaAs self-organized quantum dots density by fast growth rate. Superlattices Microstruct. **44**, 420–424 (2008)
12. S. Chakrabarti, A. Stiff-Roberts, P. Bhattacharya, S. Gunapala, S. Bandara, S. Rafol et al., High-temperature operation of InAs-GaAs quantum-dot infrared photodetectors with large responsivity and detectivity. IEEE Photonics Technol. Lett. **16**, 1361–1363 (2004)
13. J. Phillips, P. Bhattacharya, S. Kennerly, D. Beekman, M. Dutta, Self-assembled InAs-GaAs quantum-dot intersubband detectors. IEEE J. Quantum Electron. **35**, 936–943 (1999)
14. D. Pan, E. Towe, S. Kennerly, A five-period normal-incidence (In, Ga) As/GaAs quantum-dot infrared photodetector. Appl. Phys. Lett. **75**, 2719–2721 (1999)
15. J. Tatebayashi, N. Hatori, H. Kakuma, H. Ebe, H. Sudo, A. Kuramata et al., Low threshold current operation of self-assembled InAs/GaAs quantum dot lasers by metal organic chemical vapour deposition. Electron. Lett. **39**, 1130–1131 (2003)
16. H. Liu, S. Liew, T. Badcock, D. Mowbray, M. Skolnick, S. Ray et al., p-doped 1.3 μm InAs/GaAs quantum-dot laser with a low threshold current density and high differential efficiency. Appl. Phys. Lett. **89**, 073113 (2006)
17. T. Badcock, H. Liu, K. Groom, C. Jin, M. Gutierrez, M. Hopkinson et al., 1.3 μm InAs/GaAs quantum-dot laser with low-threshold current density and negative characteristic temperature above room temperature. Electron. Lett. **42**, 922–923 (2006)
18. V. Popescu, G. Bester, M.C. Hanna, A.G. Norman, A. Zunger, Theoretical and experimental examination of the intermediate-band concept for strain-balanced (In, Ga) As/Ga (As, P) quantum dot solar cells. Phys. Rev. B **78**, 205321 (2008)

19. S. Tomic, T.S. Jones, N.M. Harrison, Absorption characteristics of a quantum dot array induced intermediate band: Implications for solar cell design. Appl. Phys. Lett. **93**, 263105–263105-3 (2008)
20. D. Bimberg, M. Grundmann, N.N. Ledentsov, *Quantum Dot Heterostructures* (Wiley, Chichester, U.K., 1999)
21. A. Mandal, U. Verma, S. Chakrabarti, Effects of ex situ annealing on quaternary alloy (InAlGaAs) capped InAs/GaAs quantum dot heterostructures on optimization of optoelectronic and structural properties with variation in growth rate, barrier thickness, and seed quantum dot monolayer coverage. Superlattices Microstruct. **58**, 101–119 (2013)
22. Z.-Y. Xu, Z.-D. Lu, X. Yang, Z. Yuan, B. Zheng, J. Xu et al., Carrier relaxation and thermal activation of localized excitons in self-organized InAs multilayers grown on GaAs substrates. Phys. Rev. B **54**, 11528 (1996)
23. S. Adhikary, N. Halder, S. Chakrabarti, S. Majumdar, S. Ray, M. Herrera et al., Investigation of strain in self-assembled multilayer InAs/GaAs quantum dot heterostructures. J. Cryst. Growth **312**, 724–729 (2010)
24. J. Suseendran, N. Halder, S. Chakrabarti, T. Mishima, C. Stanley, Stacking of multilayer InAs quantum dots with combination capping of InAlGaAs and high temperature grown GaAs. Superlattices Microstruct. **46**, 900–906 (2009)
25. S. Adhikary, K. Ghosh, S. Chowdhury, N. Halder, S. Chakrabarti, An approach to suppress the blue-shift of photoluminescence peaks in coupled multilayer InAs/GaAs quantum dots by high temperature post-growth annealing. Mater. Res. Bull. **45**, 1466–1469 (2010)

Chapter 4
Effects of Low Energy Light Ion (H^-) Implantations on Quaternary-Alloy-Capped InAs/GaAs Quantum Dot Infrared Photodetectors

Abstract In Chap. 2, we showed that heavy ion (S^-) implantations actually degraded the material and structural quality of InAs/GaAs QD systems, while there was an improvement in material quality when implanted with light ions (H^-). We, therefore, decided to validate these results and study the effects of H^- ion implantation on In(Ga)As/GaAs QD devices. Our research of interest was intersubband detectors. To validate the impact of ion implantation over devices, quaternary alloy-capped InAs/GaAs QDIP devices were implanted with low energy light ions (H^-). Different steps to fabricate single-pixel devices are also discussed in this chapter. A suppression of dark current density was observed for the implanted devices. Moreover, we optimized the different properties of quaternary-alloy-capped multilayer InAs/GaAs QDs in Chap. 3. The use of growth engineering and implantation techniques introduced in this study made us expect better electrical characteristics from high-quality, well-formed dots.

Keywords Intersubband detectors · *I–V* characterization · Dark current density · LO phonons · Single-pixel devices · Field-assisted tunnelling emissions

4.1 Introduction: Basic Operation of Intersubband Detectors

For a better understanding of the advantages of QDIPs, we need to understand the basic operational principles of an intersubband detector [1]. Both the working principles of QWIPs (quantum well infrared photodetectors) and QDIPs imply intersubband transitions. Basic QWIP and QDIP structures are shown in Fig. 4.1 [1]. The structures are similar in all aspects other than the fact that QDIPs have QDs in the active region while QWIPs have QWs. Figure 4.2 shows the schematic

Portions of this chapter is reprinted from **A. Mandal** et al., "Proposed mechanism to represent the suppression of dark current density by four orders with low energy light ion (H^-) implantation in quaternary alloy-capped InAs/GaAs quantum dot infrared photodetectors," ***Materials Research Bulletin***, Vol. 48, pp. 2886–2891, 2013, with permission from Elsevier.

© Springer Nature Singapore Pte Ltd. 2017

A. Mandal and S. Chakrabarti, *Impact of Ion Implantation on Quantum Dot Heterostructures and Devices*, DOI 10.1007/978-981-10-4334-5_4

structure and simplified band diagram of an InAs/GaAs QDIP, consists of vertically stacked InAs quantum dots layers with GaAs capping layers. The electrons are excited by the normal incident light, are subsequently collected through the top contact layer electrode and thus generate a photocurrent. This is a unipolar photodetector (involving only electrons or holes). Only the conduction band is involved in the photodetection and photocurrent generation process. To take advantage of the higher electron mobility, most of the intersubband detectors (especially QDIPs) grown are of *n*-type [1].

4.2 Advantages of QDIPs

Over the past two decades, rapid progress in the growth of self-assembled quantum dots has facilitated their applications in high-performance optoelectronic devices such as QDIPs [2, 3]. QDIPs have several advantages over QWIPs and other types of IR detectors. QDIPs have emerged superior to QWIPs due to their intrinsic sensitivity to the normally incident infrared (IR) light and significantly low dark current [2].

Due to the energy quantization in all three dimensions, thermal generation of carriers is significantly suppressed in QDIPs. As a result, the electron relaxation time from excited states is enhanced due to phonon bottleneck [4, 5]; i.e. carrier lifetime is increased. Further, generation by LO phonons is prohibited in QDIP unless the gap between the discrete energy levels exactly equals that of the phonon. This prohibition does not apply to quantum wells, since the levels are quantized only in the growth direction and a continuum exists in the other two directions. So, the generation–recombination by LO phonons does occur frequently in QW structures. As a result, QDIPs are always expected to deliver a larger signal-to-noise ratio compared to QWIPs. Thus, the large responsivity and high detectivity of QDIPs are attributed to their three-dimensional carrier confinement and phonon bottlenecks [4, 5].

These characteristics made QDIPs suitable for use in high-resolution and high-sensitivity photodetection in the mid-wavelength infrared (MWIR) and long-wavelength infrared (LWIR) regions [6]. In general, multicolour IR detectors

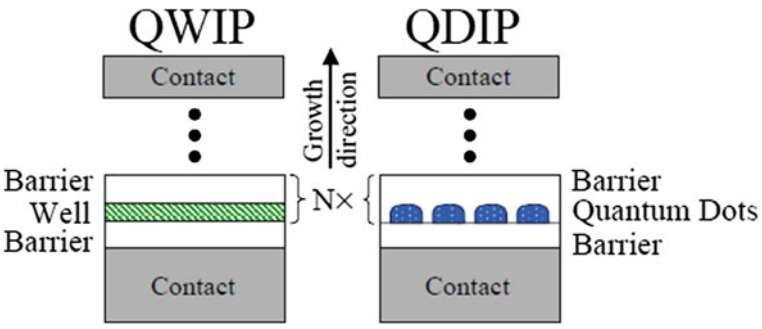

Fig. 4.1 Basic heterostructures of quantum well and quantum dot infrared photodetectors (QWIPs and QDIPs)

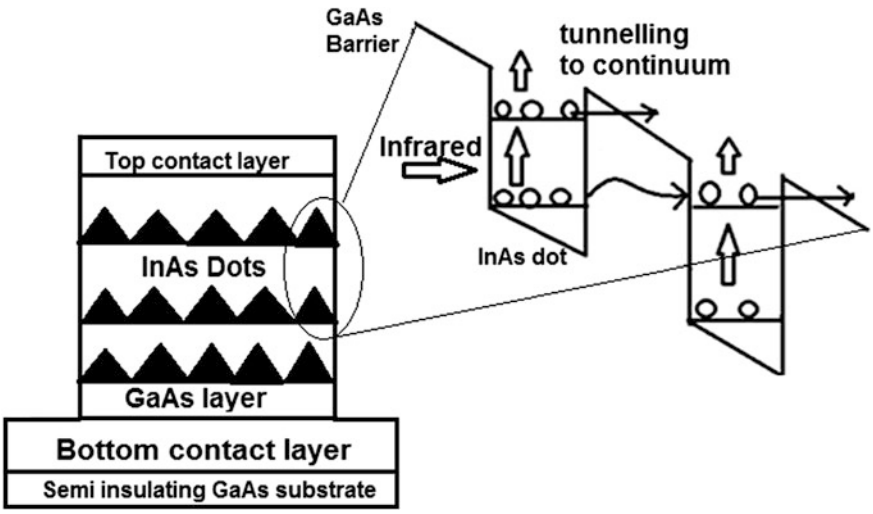

Fig. 4.2 Schematic structure of an InAs/GaAs quantum dot infrared photodetector (QDIP) and a simplified band diagram to show its basic operation

are more favourable and highly desirable for advanced sensing and imaging systems [7, 8] because of their narrow distribution in discrete energy states and narrower spectrum width at the detective wavelength; here too, QDIPs are a better option than QWIPs [7]. Growth engineering for QWIPs and their fabrications is complex [7, 8] and leaves room for QDIPs as a better application.

4.3 Previously Reported Results on In(Ga)As/GaAs QDIPs

Several groups working on In(Ga)As/GaAs QDIPs have the common aim of realizing room-temperature operation with high device performance. The atmospheric windows of interest for these QDIPs are mainly the mid-infrared range of 3–5 μm [9] and far-infrared range of 8–14 μm [10, 11]. The generation of high dark current at high temperature is the main challenge in producing high-temperature QDIP operation and better performance characteristics such as high detectivity and responsivity.

Drexler et al. first presented results which were interpreted as far-infrared absorption for charged InGaAs QDs at longer wavelength [12], whereas Fricke et al. realized far-infrared absorption in charged InAs QDs [13]. Results on mid-infrared photoconductivity in InAs quantum dots were first reported by Berryman et al. [9]; they achieved several apparent peaks near 2.8, 3.2 and 3.9 μm at 80 K. Soon after, Pan et al. reported a peak detectivity of 1×10^{10} cm-Hz$^{1/2}$/W for 13 μm response at

40 K [14] and Phillips et al. reported photoconductivity signal peak at 17 μm from an n-i-n InAs/GaAs detector structure [15]. Subsequently, several QDIP designs have been proposed by different groups. Stiff-Roberts et al. utilized an AlGaAs barrier layer within QDIPs [16] and attained a specific detectivity of 3×10^9 cm-$Hz^{1/2}$/W at 100 K. Ye et al. used an InGaAs capping in the active region [17] and obtained a responsivity of 22 mA/W and peak detectivity of 3.2×10^9 cm-$Hz^{1/2}$/W at 77 K. With a dot-in-a-well (DWELL) QDIP structures [18], Gunapala et al. obtained a peak detectivity of 10^{10} cm-$Hz^{1/2}$/W at 77 K for a 8.1-μm device.

Using tunnel barriers of AlGaAs in InGaAs/GaAs QDIP structures, Bhattacharya et al. reported high-temperature (240–300 K) operation for these QDIPs [19]. They received two colour photo-responses at the wavelengths 6 and 17 μm and extremely low dark current density of 1.55 A/cm^2 at 300 K. Tunnelling barriers were responsible for the generation of such a low dark current density. For 17-μm absorption, the measured peak responsivity was 0.16 A/W (300 K) and the specific detectivity was 1.5×10^7 cm-$Hz^{1/2}$/W at 280 K. For the 6 μm absorption, specific detectivity was 2.4×10^{10} cm-$Hz^{1/2}$/W at 80 K [19].

However, the device performance levels of the available IR photodetectors are still not satisfactory. Chakrabarti et al. [20] developed an uncoupled InGaAs/GaAs QD heterostructure where the InGaAs dots were capped with a relatively thick combination barrier comprising a 30-Å layer of quaternary $In_{0.21}Al_{0.21}Ga_{0.58}As$ and a 500-Å layer of GaAs. From this 35-layer InGaAs/GaAs QDIP heterostructure, they obtained a high detectivity of 1.01×10^{11} cm-$Hz^{1/2}$/W for the 10.2-μm response at 77 K. The device also produced detectivity of the order of 6.4×10^{10} cm-$Hz^{1/2}$/W at 100 K. The thick barrier in this QD heterostructure was the hindrance for carrier tunnelling in adjacent dot layers at high temperature, and a low dark current density of 1.36×10^{-6} A/cm^2 at 77 K was thus achieved.

In this current study, the QDIP performances we achieved from In(Ga)As/GaAs QDIPs are not as good as the results mentioned above. The probable reasons might be the usual low fill factor (20–25%) of QDs [21] and presence of high defect density in a strained system [22]. So, to improve the material quality and QDIP characteristics, we need to eradicate these defects from the heterostructures, as concluded in this chapter. Here, we had tried to improve the In(Ga)As/GaAs QDIP performances by low energy light ion (H^-) implantation.

4.4 Growth of Quaternary Alloy-Capped InAs/GaAs QDIPs

InAs/GaAs-based n-i-n QDIP, heterostructures (Fig. 4.3) were grown over semi-insulating GaAs (100) substrates using a solid source MBE system (Riber SYS14020 Epineat III–V). First, a 200-nm GaAs buffer layer was grown at 590 °C

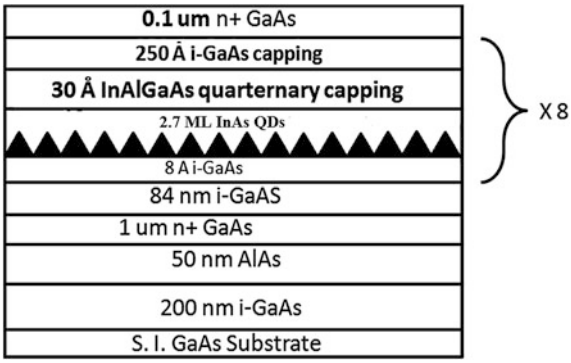

Fig. 4.3 Heterostructure of quaternary-alloy-capped 8-layered n-i-n InAs/GaAs quantum dot infrared photodetector (QDIP) [24]

temperature followed by the *n*-type bottom contact. The bottom contact was a Si-doped GaAs layer of 1-μm thickness. The growth temperature was then brought down to 500 °C to start the growth of the active region and also to avoid In–Ga intermixing at the dots. A higher growth rate of 0.2 ML/s was maintained for growing 2.7 ML InAs QDs. The QDs were further capped using a combination of a 30-Å quaternary ($In_{0.21}Al_{0.21}Ga_{0.58}As$) layer and a 250-Å GaAs layer. The QD and the combination capping were repeated for eight periods. As we found from TRIM calculation that hydrogen ions of 50 keV energy can penetrate up to a depth of 3605 Å [23], eight growth periods were performed so that all of the QD layers experienced the effects of ion implantation. At the end of eight periods, the device structure was completed by growing an *n*-type top contact of 0.1-μm thickness.

4.5 Optimization of H^- Ion Fluence and Implantation

For a better understanding of the effect of H^- ion implantation over quaternary alloy-capped QDIPs and to optimize the fluences of H^- ions, we tried implantation over a single layered structure first using LEAF. Figure 4.4 shows the heterostructure.

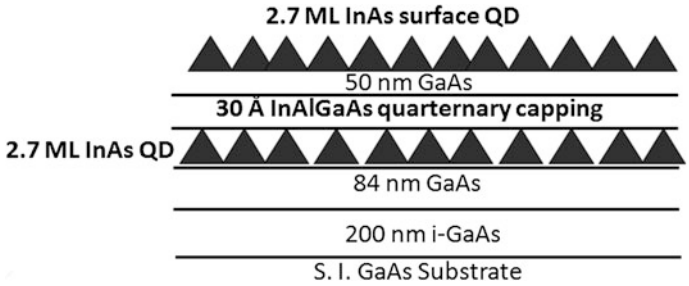

Fig. 4.4 Heterostructure of quaternary-alloy (InAlGaAs) capped single-layer InAs/GaAs quantum dot (QD) used for optimizing fluence of H^- ion implantation

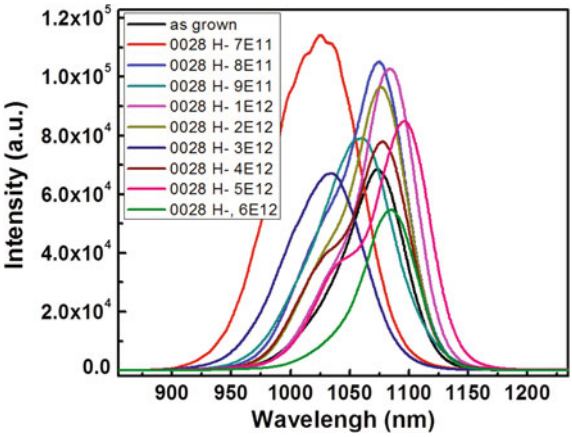

Fig. 4.5 Room-temperature photoluminescence (PL) peaks from quaternary-alloy-capped single-layer InAs/GaAs quantum dot (QD) heterostructures implanted with 50 keV H^- ions of fluence varying between 7×10^{11} and 6×10^{12} ions/cm^2

Implantation was performed over the heterostructures with 50 keV H^- ions of fluence varying between 7×10^{11} and 6×10^{12} ions/cm^2. The samples implanted with the fluences of 8×10^{11}, 1×10^{12} and 2×10^{12} ions/cm^2 gave the best results as their room temperature PL showed (Fig. 4.5) an increase in PL intensity with almost no shift in peak position. Thus, we optimized these three fluences as the ideal values for the implantation study of quaternary-alloy-capped InAs/GaAs QDIPs. Next, the QDIP structures (Fig. 4.3) were implanted with 50 keV H^- ions of optimized fluence values.

4.6 Fabrication of Mesa-Shaped Single-Pixel Devices on Implanted Samples

For performing *I–V* characterization, single-pixel devices had to be fabricated out of the QDIP heterostructures (Fig. 4.3). Figure 4.6 shows the cross section of an ideal single-pixel device after the fabrication is performed and it is ready for electrical measurements. Once the ion implantation was done, both un-implanted and implanted structures (Fig. 4.3) were subjected to device fabrication.

The fabrication of these devices requires two steps of lithography for making metal contacts. The different fabrication steps of this structure are as follows:

(1) **Surface cleaning**: The samples were dipped in trichloroethylene (TCE), acetone and isopropyl alcohol (IPA) in sequence for three minutes each and then rinsed with deionized (DI) water for 1 min.

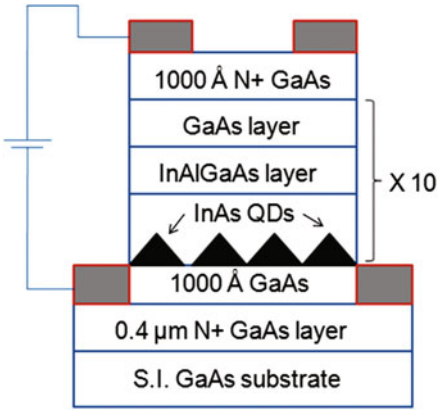

Fig. 4.6 Heterostructure of a single-pixel device after fabrication

(2) **Mesa definition (lithography)**: The steps for mesa formation are discussed below.

(a) Samples were kept for dehydration baking for 6 min at 150 °C for absorbing the moisture from the sample surface.
(b) Spinning was then performed with positive photo resist (PPR) "SPR-700-1.8" at 3000 rpm for 30 s.
(c) Samples were prebaked for 3 min at 90 °C for PPR hardening.
(d) Samples were then exposed to UV light of 16 mJ/cm^2 energy density for 3.3 s.
(e) Next, samples were developed with "MF319" NaOH solution for 60 s. Figure 4.7 shows how the structures looked post development.

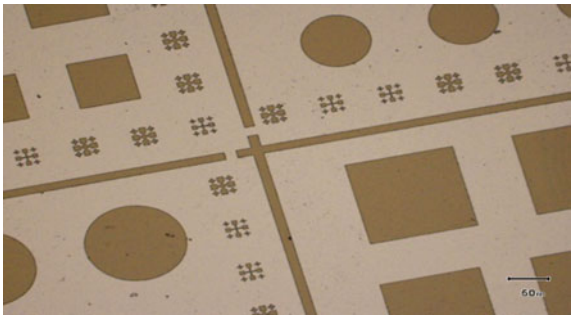

Fig. 4.7 Picture taken after mesa lithography of devices

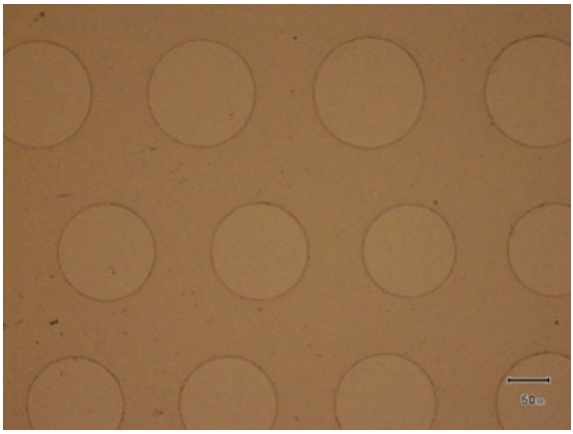

Fig. 4.8 After wet etching, the structures are ready for contact definition

(3) **Wet etching**: The samples were dipped in an H_3PO_4:H_2O_2:DI H_2O (3:1:20) solution; etch rate was 0.335 µm/min; remaining resist was removed by acetone. Figure 4.8 shows the structures after wet etching.

(4) **Contact definition (lithography)**: The lithography steps for contact definition are as mentioned below.

(a) Samples were kept for dehydration baking for 6 min at 150 °C for absorbing the moisture from the sample surface.
(b) Spinning was then performed with PPR at 3000 rpm for 30 s.
(c) Prebaking for 3 min at 90 °C helped in hardening the PPR.
(d) Next, samples were exposed to UV light of 16 mJ/cm^2 energy density for 3.5 s.

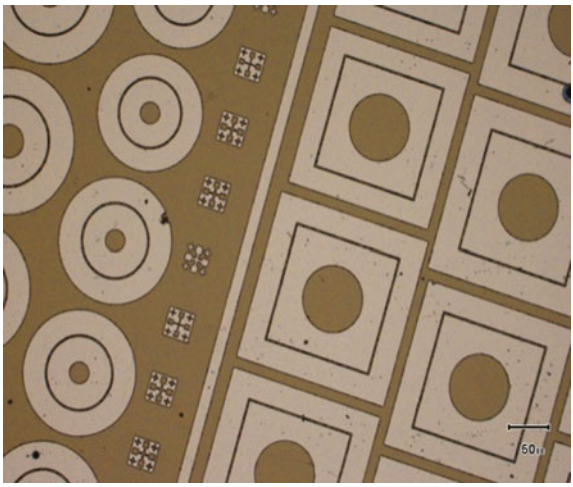

Fig. 4.9 Picture taken after contact lithography during device fabrication

(e) Further, samples were developed with "MF319" NaOH solution for 60 s. Figure 4.9 shows the picture after contact definition.

(5) **Metallization and lift-off**: As we know, the best technique for producing an ohmic contact is to position it in very highly doped region, so that there is almost zero potential barrier at the junction, and very high transparency for the carriers to flow [25]. As suggested in prior literature [25, 26], a AuGe/Ni/Au metal stack of 50/25/200 nm thickness was deposited over $n+$ GaAs by a four-target e-beam evaporator at a vacuum pressure of about 10^{-6} mbar. The eutectic temperature of the AuGe alloy is 361 °C. AuGe metal has the tendency to ball up, and, therefore, the morphology of the contact is poor; this may be prevented with the introduction of Ni over layer. Ni also forms few electrically important binary and ternary compounds by reacting with GaAs at low temperatures [26]. After metallization is performed, we kept the samples in acetone and sonicated them to lift off the metal from other regions except the devices. Figure 4.10 shows the single-pixel devices after metallization and lift-off are performed.

(6) **Rapid thermal annealing and wire bonding**: Although the metal stack of AuGe/Ni/Au has a well-improved morphology, AuGe has a tendency of forming the compound AuGa after reacting with GaAs, which is responsible for spiking and poor morphology. This can be avoided by rapid thermal annealing, where the formation of AuGa is limited and thus the chance of total consumption of gold from the contact is decreased [26]. Rapid thermal annealing was carried out at 380 °C for 60 s in an argon (Ar) atmosphere. The annealing was done under GaAs proximity capping in order to prevent the degradation of sample quality due to out-diffusion of As from the sample surface.

Once rapid thermal annealing is performed, the devices are fixed on to a 64-pin leaded chip carrier (LCC) using E1172A epoxy and cured for 20 min at 135 °C. Then, top and bottom contacts of the devices are wire bonded (gold wire) to respective LCC pads at 75 °C with an ultrasonic power of 40 mW for 10 ms. Figure 4.11 shows the contacts of the devices wire bonded with the LCC pad.

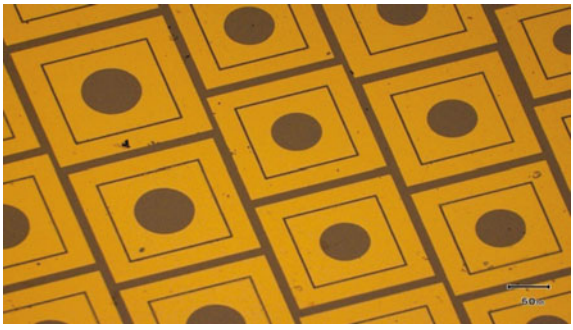

Fig. 4.10 Prominent mesa-shaped single-pixel devices after metallization

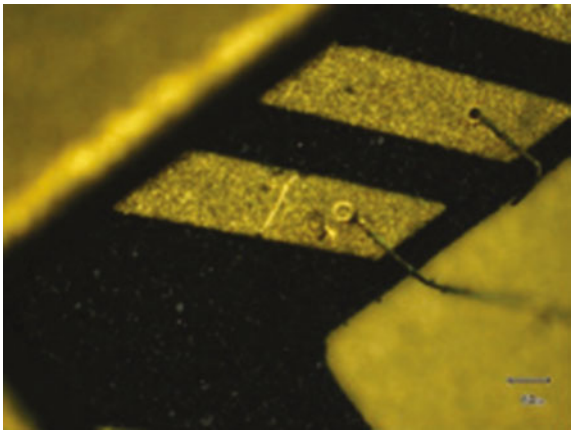

Fig. 4.11 Contacts of devices are wire bonded with leaded chip carrier (LCC) pad

4.7 Different Characterizations Performed for Implanted QDIPs

The optical and material characteristics of the devices were studied using low-temperature PL. The PL experiments were carried out using a 532-nm excitation source. Conventional photolithography, wet etching and metal evaporation techniques were used to fabricate mesa-shaped devices with 300-μm diametres (Sect. 4.6). Temperature-dependent *I–V* measurements were then obtained using a Keithley 2400 source metre.

4.8 Results and Discussion

4.8.1 Optical and Structural Properties of H^- Ion-Implanted InAs/GaAs QDIPs

The low-temperature (8 K) photoluminescence study depicted an enhancement in PL emission with H^- ion implantation up to a fluence of 2×10^{12} ions/cm^2 (Fig. 4.12). Annihilation of defects due to light ion implantation could be responsible for this enhancement, i.e. more radiative recombination (Sect. 2.5.2). Simultaneously, a blue shift in PL emission was also observed for the implanted samples. As almost the whole heterostructure is experiencing the light ion implantation, a low degree of In–Ga intermixing might be responsible for this blue shift.

However, the dots were detected as bimodal in both as-grown and implanted samples when their PL emissions at 8 K were recorded with lowest excitation

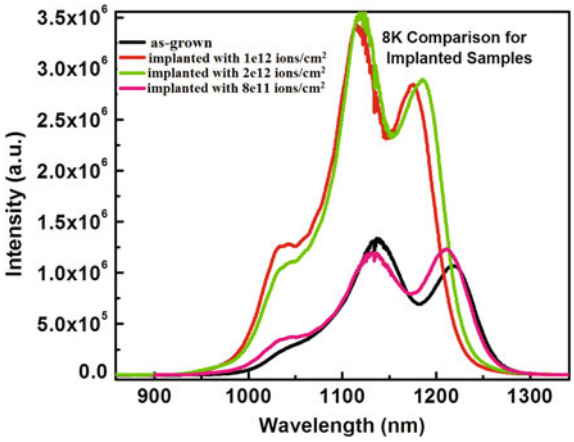

Fig. 4.12 Photoluminescence (PL) comparisons at 8 K for as-grown and implanted quaternary alloy capped InAs/GaAs quantum dot infrared photodetectors (QDIPs) [24]

power of 500 μW (Fig. 4.13). Peak P1 denotes larger dots while peak P2 denotes smaller dots in Fig. 4.13.

When AFM was performed to study the surface morphology for the same kind of single-layer structure, a clearer presence of both larger (spotted) and smaller dots was observed with a dot density of 9×10^9 dots/cm^2 and 5×10^9 dots/cm^2, respectively (Fig. 4.14). Assuming a lower coupling effect and the lack of vertical alignment due to a thicker capping layer [27], we can hint at the dominance of larger dots in the multilayer structures under observation. When FWHM from low-temperature PL study was compared for both the dot families, the homogeneity

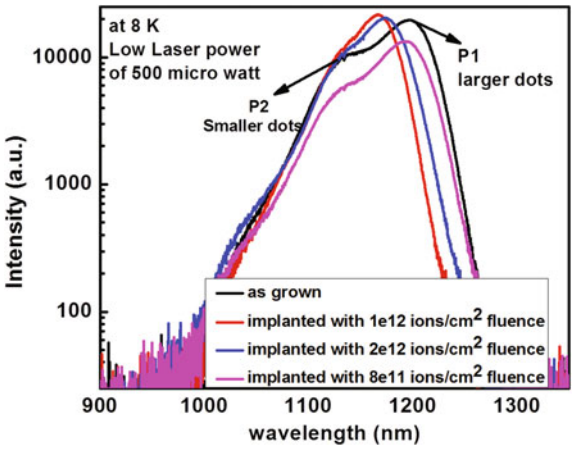

Fig. 4.13 Photoluminescence (PL) comparisons at 8 K for as-grown and implanted samples at the lowest excitation power of 500 μW [24]

of larger dots observed attributed to the narrower FWHM of PL emissions [28] (Fig. 4.15).

4.8.2 *Electrical Properties of H^- Ion-Implanted InAs/GaAs QDIPs*

The main causes of dark current generation are thermionic emission, thermally assisted tunnelling, sequential tunnelling and, most importantly, field-assisted tunnelling of carriers under high bias [29]. Figure 4.16 shows the different processes of dark current generation from the conduction band of the InAs/GaAs QDs.

Temperature-dependent *I–V* measurements were performed for all of the devices under study. Figure 4.17 depicts the variations in dark current density with bias for all of the devices at 77 K. With implantation, dark current density decreased up to the fluence of 1×10^{12} ions/cm^2 by four orders (3.7×10^{-6} A/cm^2 at 0.4 V). Although there is a further enhancement in dark current density with fluence, it is less than that of the as-grown device (2×10^{-2} A/cm^2 at 0.4 V).

Figure 4.18 represents the activation energies at both positive and negative bias for the as-grown and implanted samples at 77 K. Activation energy calculated for the as-grown sample was 155 meV at zero bias and increased further with increase in fluence up to 1×10^{12} ions/cm^2 (294 meV). Increase in activation energy demonstrates better carrier confinement within the dots, which also supports the reduction in dark current density for that sample. Also, we may assume that eradication of defects due to light ion implantation helped in reducing the dark current densities of implanted devices. These defects present in capping layer and in

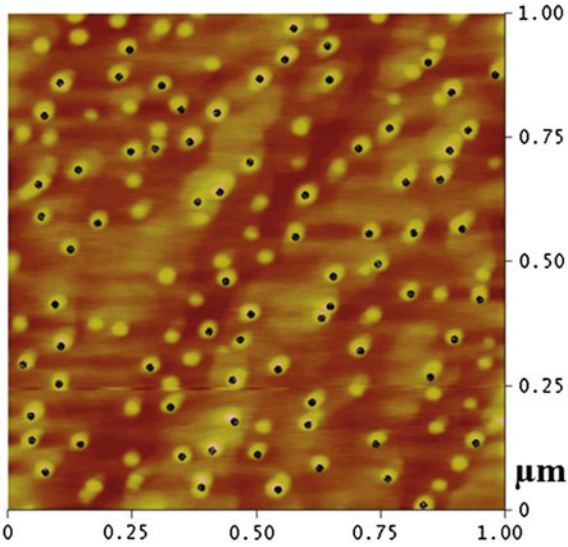

Fig. 4.14 Atomic force microscopy (AFM) image of quaternary-alloy-capped single-layer InAs/GaAs quantum dots to study surface morphology. The *black spotted dots* are larger in size [24]

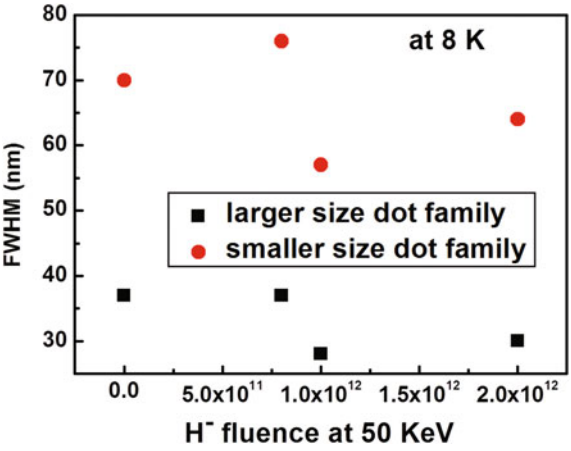

Fig. 4.15 Variation of full width at half maximum (FWHM) of photoluminescence (PL) emission with implantation (fluence values of 50 keV H^- ions) for smaller and larger dot families [24]

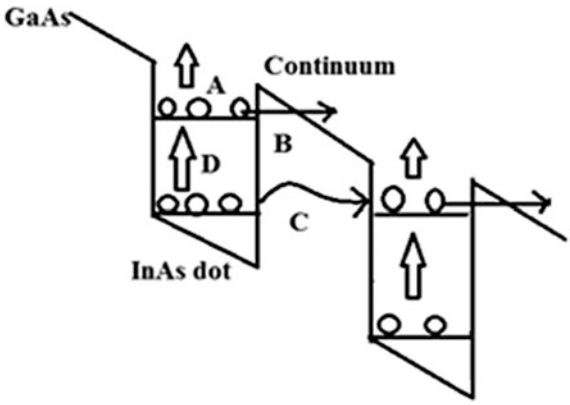

Fig. 4.16 Different sources of dark current generation: thermionic emission (**a**), field-assisted tunnelling (**b**), sequential tunnelling (**c**) and thermally assisted tunnelling (**d**) [24]

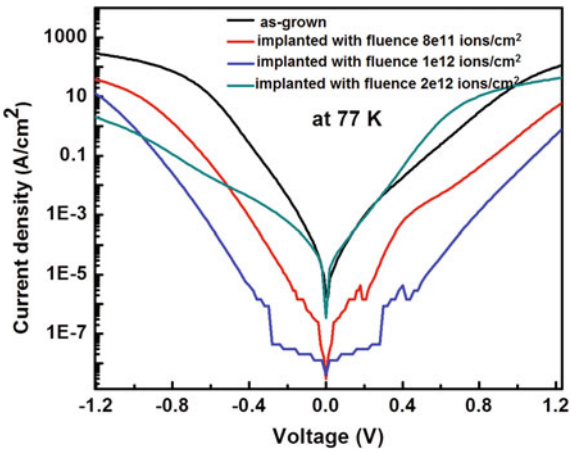

Fig. 4.17 Variation of dark current density with bias at 77 K for the as-grown and implanted InAs/GaAs quantum dot (QD) detectors [24]

the vicinity of dots can preserve carriers which can further be emitted to the continuum by thermionic emission. Therefore, these carriers originating at defects could also generate the dark current originally suppressed by light ion implantation.

Figure 4.17 also shows that for the sample implanted with 1×10^{12} ions/cm^2 fluence, within the bias of 0.35 V, the dark current density increases very slowly; however, as more bias is applied, the current density increases steeply. This phenomenon strongly supports the lowering of the potential barrier φ_B within a higher applied bias range [30]. Stiff-Roberts et al. reported the Wentzel–Kramer–Brillouin approximation for the rate of field-assisted tunnelling emission G_t (in conduction band) through a one-dimensional triangular barrier (Fig. 4.16) towards the continuum as [29]:

$$G_t = G_{to} \exp\left[(-4/3)\left\{(\sqrt{2}\sqrt{q}\sqrt{m^*})/\hbar\right\}\left\{3\sqrt{\varphi_B}/E\right\}\right] \exp\{\Delta\varepsilon/(K_B T)\} \exp\left[\left(\pi\hbar^2\langle N\rangle\right)/\left(m^* K_B T \alpha^2\right)\right] \tag{4.1}$$

where G_{to} is the field-assisted tunnelling emission rate constant, q is the charge of the electron, m^* is the electron effective mass, E is the effective field, $\hbar$ is Planck's constant, K_B is the Boltzmann constant, φ_B is the potential barrier, N is the number of electrons that occupy the dot, $\Delta\varepsilon$ is the energy difference from the quantum dot ground state to the highest filled quantum dot energy level and α is the dot width. Further, the potential barrier φ_B can be expressed as [29]:

$$\varphi_B = (\varepsilon_{QD} - \Delta\varepsilon)/q \tag{4.2}$$

where ε_{QD} is the ground state ionization energy of the dot [29]. Using Eq. (4.1), we can see that both the increase in the parameter E and the lowering of φ_B do enhance the dark current densities due to field-assisted tunnelling emission at higher bias, which supports our results. Moreover, we cannot ignore the effect of In–Ga intermixing within the dot due to implantation [31], and the slight PL blue shift depicted

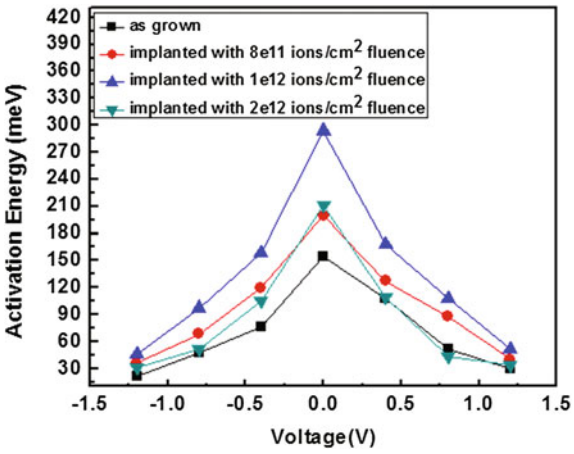

Fig. 4.18 Variation of activation energies at both positive and negative bias for the as-grown and implanted InAs/GaAs quantum dot (QD) detectors at 77 K [24]

in Fig. 4.12 supports this fact. The greater intermixing at higher fluences can result in a lowered φ_B value in Eq. (4.2) and also enhance the process of field-assisted tunnelling emission. These unwanted phenomena gave rise to high dark current density for the sample implanted with 2×10^{12} ions/cm^2 fluence (Fig. 4.17).

4.9 Significant Results from H^- Ion-Implanted InAs/GaAs QDIPs and Conclusions

The effects of H^- ion implantation on the material, structural and electrical characteristics of quaternary alloy-capped InAs/GaAs QDIPs were demonstrated in this chapter. Dark current density was suppressed up to four orders within implanted devices. We assumed both, eradication of defects and In–Ga intermixing attributed to light ion implantation, were mainly responsible for this dark current density suppression. This study definitely paves the way for the improvement of electrical carrier transport in InAs/GaAs QDIPs with low energy light ion implantation. However, the results were still not satisfactory as we could not record any photo-response from these devices; there was no dominance of photogenerated carriers. We suspect that the sequential tunnelling (Fig. 4.16) of dark current generation was responsible. Probably, the total capping layer thickness of 280 Å was not enough to prevent sequential tunnelling. Therefore, we next grew QDs with thicker barrier layer for better device performance as compared to these QDIPs, as presented in next chapter.

References

1. M. Razeghi, *Technology of Quantum Devices* (Springer, New York, USA, 2010)
2. L. Fu, H. Tan, I. McKerracher, J. Wong-Leung, C. Jagadish, N. Vukmirović et al., Effects of rapid thermal annealing on device characteristics of InGaAs/GaAs quantum dot infrared photodetectors. J. Appl. Phys. **99**, 114517 (2006)
3. S. Xu, S. Chua, T. Mei, X. Wang, X. Zhang, G. Karunasiri et al., Characteristics of InGaAs quantum dot infrared photodetectors. Appl. Phys. Lett. **73**, 3153–3155 (1998)
4. H. Liu, Quantum dot infrared photodetector. Optoelectron. Rev. **11**, 1–6 (2003)
5. P. Martyniuk, A. Rogalski, Quantum-dot infrared photodetectors: status and outlook. Progress Quantum Electron. **32**, 89–120 (2008)
6. S. Chakrabarti, X. Su, P. Bhattacharya, G. Ariyawansa, A.U. Perera, Characteristics of a multicolor InGaAs-GaAs quantum-dot infrared photodetector. IEEE Photonics Technol. Lett. **17**, 178–180 (2005)
7. S.M. Kim, J.S. Harris, Multicolor InGaAs quantum-dot infrared photodetectors. IEEE Photonics Technol. Lett. **16**, 2538–2540 (2004)
8. X. Jiang, S.S. Li, M.Z. Tidrow, Investigation of a multistack voltage-tunable four-color quantum-well infrared photodetector for mid-and long-wavelength infrared detection. IEEE J. Quantum Electron. **35**, 1685–1692 (1999)
9. K.W. Berryman, S.A. Lyon, M. Segev, Mid-infrared photoconductivity in InAs quantum dots. Appl. Phys. Lett. **70**, 1861–1863 (1997)

10. E.-T. Kim, A. Madhukar, Z. Ye, J.C. Campbell, High detectivity InAs quantum dot infrared photodetectors. Appl. Phys. Lett. **84**, 3277–3279 (2004)
11. J.W. Kim, J.E. Oh, S.C. Hong, C.H. Park, T.K. Yoo, Room temperature far infrared (8/spl sim/10 μm) photodetectors using self-assembled InAs quantum dots with high detectivity. IEEE Electron Device Lett. **21**, 329–331 (2000)
12. H. Drexler, D. Leonard, W. Hansen, J.P. Kotthaus, P.M. Petroff, Spectroscopy of quantum levels in charge—tunable InGaAs quantum dots. Phys. Rev. Lett. **73**, 2252–2255 (1994)
13. M. Fricke, A. Lorke, J.P. Kotthaus, G. Medeiros-Ribeiro, P.M. Petroff, Shell structure and electron-electron interaction in self-assembled InAs quantum dots. Europhys. Lett. **36**, 197 (1996)
14. D. Pan, E. Towe, S. Kennerly, Normal-incidence intersubband (In, Ga)As/GaAs quantum dot infrared photodetectors. Appl. Phys. Lett. **73**, 1937–1939 (1998)
15. J. Phillips, K. Kamath, P. Bhattacharya, Far-infrared photoconductivity in self-organized InAs quantum dots. Appl. Phys. Lett. **72**, 2020–2021 (1998)
16. A. Stiff-Roberts, S. Krishna, P. Bhattacharya, S.W. Kennerly, Normal-incidence, high-temperature, mid-infrared, InAs-GaAs vertical quantum-dot infrared photodetector. IEEE J. Quantum Electron. **37**, 1412–1419 (2001)
17. Z. Ye, J.C. Campbell, Z. Chen, E.-T. Kim, A. Madhukar, InAs quantum dot infrared photodetectors with InGaAs strain-relief cap layers. J. Appl. Phys. **92**, 7462 (2002)
18. S.D. Gunapala, S.V. Bandara, C.J. Hill, D.Z. Ting, J.K. Liu, B. Rafol et al., 640 × 512 pixels long-wavelength infrared (LWIR) quantum-dot infrared photodetector (QDIP) imaging focal plane array. IEEE J. Quantum Electron. **43**, 230–237 (2007)
19. P. Bhattacharya, X. Su, S. Chakrabarti, G. Ariyawansa, A. Perera, Characteristics of a tunneling quantum-dot infrared photodetector operating at room temperature. Appl. Phys. Lett. **86**, 191106–191106-3 (2005)
20. S. Chakrabarti, S. Adhikary, N. Halder, Y. Aytac, A. Perera, High-performance, long-wave (∼10.2 μm) InGaAs/GaAs quantum dot infrared photodetector with quaternary In0.21Al0.21Ga0.58As capping. Appl. Phys. Lett. **99**, 181102–181102-3 (2011)
21. A. Mandal, A. Agarwal, H. Ghadi, K.C. Goma Kumari, A. Basu et al., More than one order enhancement in peak detectivity (D*) for quantum dot infrared photodetectors implanted with low energy light ions (H^-). Appl. Phys. Lett. **102**, 051105 (2013)
22. M. Sugawara, *"Self-assembled InGaAs/GaAs Quantum Dots", Semiconductors and Semimetals*, vol. 60 (Academic Press, New York, USA, 1999)
23. J.F. Ziegler, J.P. Biersack, U. Littmark, PC Programme Package TRIM95 (1995)
24. A. Mandal, H. Ghadi, K.L. Mathur, A. Basu, N.B.V. Subrahmanyam, P. Singh, S. Chakrabarti, Proposed mechanism to represent the suppression of dark current density by four orders with low energy light ion (H^-) implantation in quaternary alloy-capped InAs/GaAs quantum dot infrared photodetectors. Mater. Res. Bull. **48**, 2886–2891 (2013)
25. V. Rideout, A review of the theory and technology for ohmic contacts to group III–V compound semiconductors. Solid-State Electron. **18**, 541–550 (1975)
26. A. Baca, F. Ren, J. Zolper, R. Briggs, S. Pearton, A survey of ohmic contacts to III–V compound semiconductors. Thin Solid Films **308**, 599–606 (1997)
27. J.-Y. Duboz, H. Liu, Z. Wasilewski, M. Byloss, R. Dudek, Tunnel current in quantum dot infrared photodetectors. J. Appl. Phys. **93**, 1320–1322 (2003)
28. S. Shah, N. Halder, S. Sengupta, S. Chakrabarti, Comparison of luminescence properties of bilayer and multilayer InAs/GaAs quantum dots. Mater. Res. Bull. **47**, 130–134 (2012)
29. A. Stiff-Roberts, X. Su, S. Chakrabarti, P. Bhattacharya, Contribution of field-assisted tunneling emission to dark current in InAs-GaAs quantum dot infrared photodetectors. IEEE Photonics Technol. Lett. **16**, 867–869 (2004)
30. J.C. Campbell, A. Madhukar, Quantum-dot infrared photodetectors. Proc. IEEE **95**, 1815–1827 (2007)
31. R. Sreekumar, A. Mandal, S. Chakrabarti, S. Gupta, Effect of heavy ion implantation on self-assembled single layer InAs/GaAs quantum dots. J. Phys. D: Appl. Phys. **43**, 505302 (2010)

Chapter 5
Effects of Low-Energy Light Ion (H^-) Implantation on Quaternary-Alloy-Capped InGaAs/GaAs Quantum Dot Infrared Photodetectors

Abstract Our main aim was to use ion implantation as an effective post-growth technique for improving the optical, electrical and spectral properties of In(Ga)As/GaAs QD heterostructures and devices. We had already seen in Chap. 2 that low-energy light ion implantation improved the material quality of InAs/GaAs QDs, whereas Chap. 4 showed that light ion implantation helped in suppression of dark current density of quaternary alloy-capped InAs/GaAs QDIPs. In order to achieve better electrical and spectral behaviour, low-energy light ion (H^-) implantations were performed over quaternary alloy-capped InGaAs/GaAs QDIPs. A reduction in dark current density along with enhanced detectivity was measured for the implanted devices as discussed in this present chapter.

Keywords InGaAs/GaAs quantum dot infrared photodetectors (QDIPs) · Spectral response · Peak detectivity · Activation energy · Mid-wavelength IR response

5.1 Scope of the Study

From the results discussed in previous chapter, we can reconsider two factors that are responsible for better device performance in QDIP heterostructures: thicker capping layer to avoid sequential tunnelling among dots (Fig. 4.16), and larger dot size to suppress field-assisted tunnelling emission of dark current generation [1]. When room temperature PL emissions of both quaternary-alloy-capped 2.7 ML InAs and 7-ML $In_{0.5}Ga_{0.5}As$ QDs were compared, it was found that lar-

Portions of this chapter is reprinted from **A. Mandal** et al., "More than one order enhancement in peak detectivity (D*) for quantum dot infrared photodetectors implanted with low energy light ions (H^-)", ***Applied Physics Letters***, Vol. 102, pp. 051105, 2013, with permission from AIP Publishing.

© Springer Nature Singapore Pte Ltd. 2017

A. Mandal and S. Chakrabarti, *Impact of Ion Implantation on Quantum Dot Heterostructures and Devices*, DOI 10.1007/978-981-10-4334-5_5

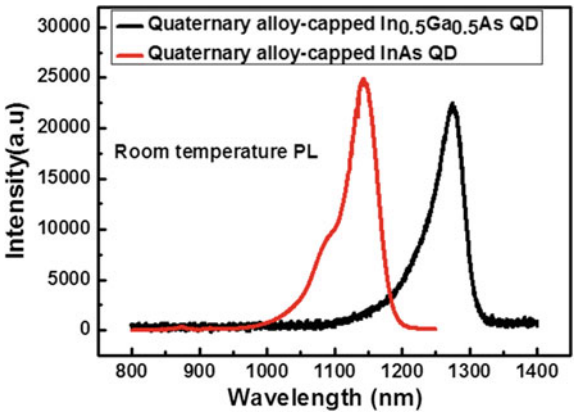

Fig. 5.1 Room temperature photoluminescence emissions from single-layer quaternary-alloy-capped InGaAs and InAs quantum dots (QDs), grown for our research purpose

ger dot size of InGaAs QDs resulted in a red shift in PL emission (Fig. 5.1). Due to the presence of less strain (i.e. less lattice mismatch) in case of InGaAs/GaAs system, more material deposition is required for the dots to evolve. Therefore, the size of InGaAs QDs is larger compared to InAs QDs. Thus, we decided to grow a QDIP heterostructure with quaternary-alloy-capped InGaAs QDs. The thickness of intrinsic GaAs capping layer was also increased to 500 Å. The QDIP heterostructures were further implanted with low-energy light ions (H^-), and different characterizations were performed on these implanted devices.

5.2 Growth of Quaternary-Alloy-Capped InGaAs/GaAs QDIPs

Quaternary-alloy-capped ten-layered $In_{0.5}Ga_{0.5}As$/GaAs-based n-i-n QDIPs (Fig. 5.2) were grown over semi-insulating GaAs (100) substrates using solid source MBE (Riber SYS14020 Epineat III–V). Initially, a 50-nm GaAs buffer layer was grown at 590 °C followed by the *n*-type bottom contact. The bottom contact was a Si-doped GaAs layer of 0.7-μm thickness. The growth temperature was then brought down to 500 °C to start the growth of the active region. A higher growth rate of 0.22 ML/s was maintained to grow 7 ML InGaAs dots. After each layer of dots, an immediate 30 Å quaternary ($In_{0.21}Al_{0.21}Ga_{0.58}As$) capping layer was grown followed by a 500 Å intrinsic GaAs capping layer. The QD and the combination capping were repeated for ten periods. At the end of the tenth layer, the device structure was completed by growing an *n*-type top contact of 0.2 μm thickness.

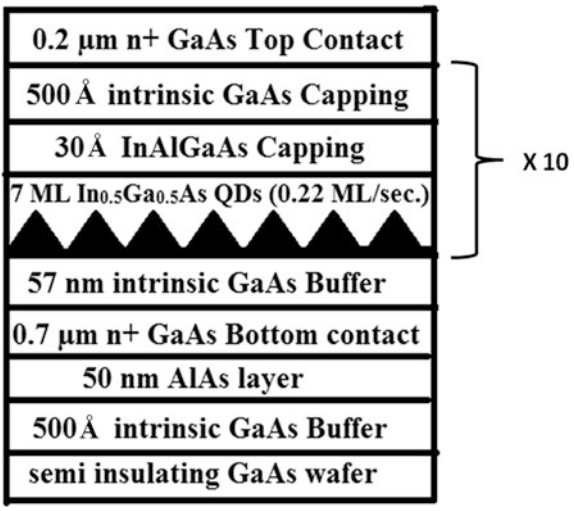
0.2 µm n+ GaAs Top Contact
500 Å intrinsic GaAs Capping
30 Å InAlGaAs Capping
7 ML In0.5Ga0.5As QDs (0.22 ML/sec.)
X 10
57 nm intrinsic GaAs Buffer
0.7 µm n+ GaAs Bottom contact
50 nm AlAs layer
500 Å intrinsic GaAs Buffer
semi insulating GaAs wafer

Fig. 5.2 Heterostructure of ten-layered quaternary alloy (InAlGaAs) capped $In_{0.5}Ga_{0.5}As/GaAs$ quantum dot infrared photodetector (QDIP) [1]

5.3 Ion Implantation, Device Fabrication and Different Characterizations for H^- Ion-Implanted InGaAs/GaAs QDIPs

Implantation of 50 keV H^- ions was conducted over these heterostructures by varying the fluence between 8×10^{11} and 2×10^{13} ions/cm^2 using LEAF; the fluence values for H^- ions are the same as those optimized in Sect. 4.5. Table 5.1 shows the sample specifications with respect to implanted fluences. Low-temperature PL experiments were carried out using a 532-nm excitation source to study the material properties of the implanted samples. Conventional photolithography, wet etching and metal evaporation techniques were used to fabricate mesa-shaped devices with 200-µm diameters [Sect. 4.6]. Temperature-dependent *I–V* measurements were performed for these devices. Low-temperature photo-responses were measured for the as-grown and implanted devices, and low-temperature detectivity was also calculated for the devices using a noise study.

Table 5.1 Implanted fluences and nomenclature for as-grown and implanted InGaAs/GaAs quantum dot infrared photodetectors (QDIPs)

Device	Implanted fluence (ions/cm^2)
Device A	As-grown
Device B	8×10^{11}
Device C	2×10^{12}
Device D	2×10^{13}

5.4 Results and Discussion

5.4.1 Optical Properties of H^- Ion-Implanted InGaAs/GaAs QDIPs

With implantation up to a fluence of 8×10^{11} ions/cm^2, enhancement of PL emission was noted for device B at room temperature (Fig. 5.3). We assumed that non-radiative recombination centres present within the dots, wetting layer and at GaAs capping layer [2, 3] of the as-grown sample absorbed most of the carriers that were responsible for radiative recombination. Upon H^- ion implantation, these non-radiative recombination centres were annihilated from the dots and their capping layers (or in the vicinity of capping layers). Thus, more carriers from the capping layer were lodged in the excited and ground states of dots before they could participate in the PL emission or radiative recombination processes [2, 3]. With further increase in fluence, the PL intensity decreased rather drastically for devices C and D (Fig. 5.3). Further increase in fluence created additional structural defects both in the GaAs barrier layer and also in the QDs [1] of device C and D. These structural defects might have acted as the sinks for the photo-excited carriers from the barrier layer and QDs. Thus, the rate of non-radiative recombination that had been enhanced in devices C and D resulted in degradation of their PL intensities.

5.4.2 Electrical Properties of H^- Ion-Implanted InGaAs/GaAs QDIPs

Low-temperature dark current densities for the as-grown and implanted devices were compared (Fig. 5.4), and a suppression of dark current density up to five

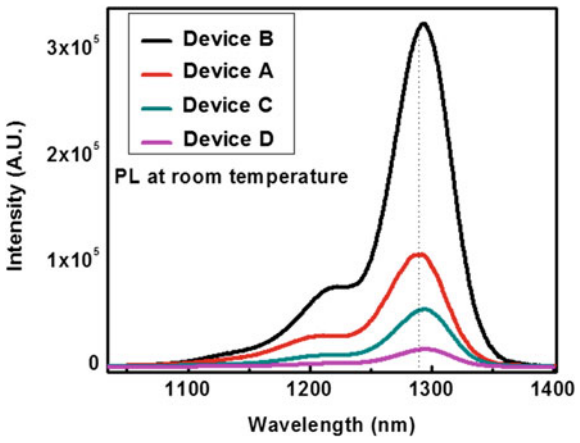

Fig. 5.3 Room temeprature photoluminescence (PL) emissions from as-grown and implanted InGaAs/GaAs quantum dot infrared photodetectors (QDIPs)

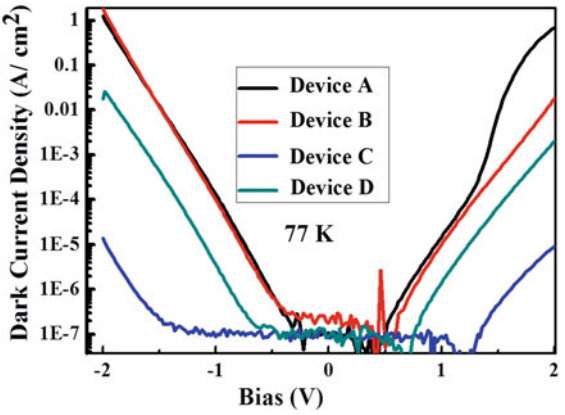

Fig. 5.4 Low-temperature (77 K) dark current density comparison of as-grown and implanted devices show decrease in dark current density of up to five orders for device C as compared to device A [1]

orders of magnitude was noticed for device C (2.2×10^{-7} A/cm^2) as compared to device A (1×10^{-2} A/cm^2), even at a high bias of −1.5 V. With further increase in fluence in case of device D, the dark current density was enhanced but remained lower than that of device A. When the bias is further increased beyond −1.5 V, due to the enhanced effective field, lowering of the potential barrier occurs in device C (Eqs. 4.1 and 4.2), which enhances the dark current density due to the field-assisted tunnelling emission, but the current density remains much lower than that of other devices.

The activation energy calculated from temperature-dependent *I–V* measurements for device A was 223 meV at zero bias, and it increased further with fluence up to 2×10^{12} ions/cm^2 (424 meV) for device C (Fig. 5.5). The increase in activation energy for the implanted devices demonstrates better carrier confinement within the dots and suggests that the dot size increases with fluence. We propose the following mechanism for these observations. The presence of quaternary phase separation alloy $In_{0.21}Al_{0.21}Ga_{0.58}As$ builds an In concentration gradient over the dots [4], while In–Al intermixing also occurs simultaneously near the dots [5]. There was a high probability that with implantation, the mobility of the Al atoms in quaternary alloy was increased, which caused them to replace the In atoms at the wetting layer [6]. These replaced In atoms diffused into the dots and dot size was increased, leading to an increase in activation energy [6]. Since the activation energy and hence dot size increases from device A to C, the barrier height for field-assisted tunnelling also increases. Increase in barrier height reduces carrier emission through the one-dimensional triangular barrier towards the continuum (Wentzel–Kramers—Brillouin approximation) [7]. With an even higher fluence of 2×10^{13} ions/cm^2 for device D, more defects were created both at the capping layer and at the dots. These defects capture most of the carriers [2, 3] before they participate in spectral response; this causes degradation in spectral characteristics and the detectivity, as discussed next.

Our study showed two colour photo-responses from these QDIP heterostructures, which strengthens the case for their use in advanced sensing and imaging

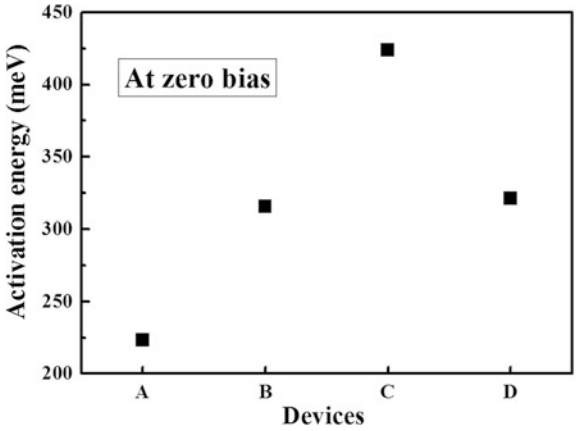

Fig. 5.5 Activation energy calculated at zero bias from temperature-dependent *I–V* measurements for as-grown device A increased up to device C [1]

applications. At higher wavelengths, the peak spectral responses were around 7.3 μm for all of the devices (peak P2 in Fig. 5.6). Moreover, the second response at the mid-wavelength IR region was near 5.5 μm (peak P1 in Fig. 5.6). The spectral width ($\Delta\lambda/\lambda$) values were measured below $\sim$0.1 for all devices. This narrow spectral width can be attributed to the bound-to-bound or bound-to-quasi-bound transitions within the dots [8, 9]. We believe that the spectral peak P2 at 7.3 μm is due to a transition from ground state to an excited state within the dot, while the peak P1 at 5.5 μm is due to transition to either a wetting layer or an InAlGaAs capping layer state.

Another very important fact was revealed, when we varied the bias for these devices while measuring their spectral responses at 77 K. We observed that devices A and C had their highest mid-wavelength IR responses at −0.5 V, while device D had its highest response at −1.0 V (Fig. 5.6). However, device B had the highest

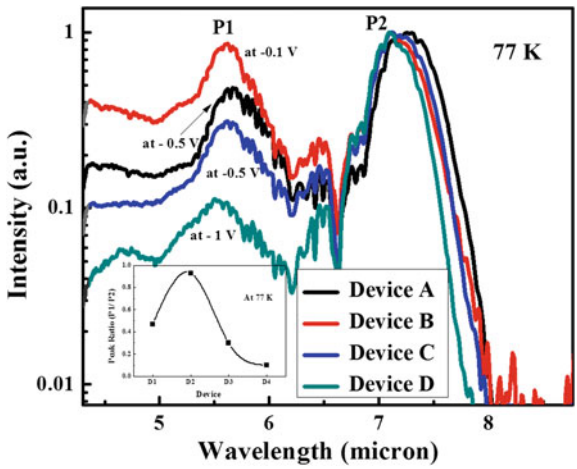

Fig. 5.6 At a low bias of −0.1 V and low temperature of 77 K, a stronger multicolour photo-response was achieved from device B. The inset shows that the peak intensity ratio of the mid-wavelength response (P1) to the long-wavelength response (P2) is highest for device B [1]

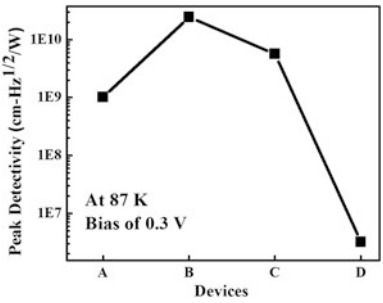

Fig. 5.7 Increase in peak detectivity (D*) by more than one order for device B at a temperature of 87 K and a bias of 0.3 V [1]

response at −0.1 V, which is greater than that from any device under study at any operational bias. Considering the best photo-responses obtained from the devices under study, the peak intensity ratio (P1/P2) of the mid-wavelength response (P1) to high-wavelength response (P2) was highest for device B, a ratio value of ∼1.0 (inset of Fig. 5.6). As such, a stronger multicolour photo-response at very low bias was achieved when the device was implanted with lower fluence. We assume that eradication of defects from the vicinity of the wetting layer of device B helped more photogenerated carriers reach the transition level before they were trapped by these defects. These "extra" photogenerated carriers resulted in high mid-wavelength IR response for device B even at a very low bias of operation. This improvement due to defect annihilation in device B can be correlated with its enhanced photoluminescence emission, as discussed in the last section.

To check the SNR within the QDIPs [8], peak detectivity (D*) values were calculated for all the devices at 87 K. D* was increased by more than one order, from $\sim 10^9$ cm-Hz$^{1/2}$/W for device A to 2.44×10^{10} cm-Hz$^{1/2}$/W for device B at a bias of 0.3 V (Fig. 5.7). However, with further increase in fluence, D* decreased to 5.66×10^9 cm-Hz$^{1/2}$/W for device C but remained greater than that of device A. Device D shows a much lower detectivity, which we believe is due to the high density of defects due to excessive implantation flux. These defects can trap the photogenerated carriers [3] and thus prevent their detection, ultimately lowering the detectivity. Another reason for the reduction in detectivity in device D is the larger dark current for this device, as discussed earlier. D* values indicate that both devices B and C are suitable for use in MWIR and LWIR regions.

5.5 Significant Results from H^- Ion-Implanted InGaAs/GaAs QDIPs and Conclusions

To our knowledge, this is probably the first study of electrical and spectral properties of low-energy H^- ion-implanted InGaAs/GaAs QDIPs. Suppression of dark current density up to five orders at high operational bias (for device C) determined the importance of H^- ion implantation as a post-growth technique to improve QDIP

performance. Device B, which was implanted with the lowest fluence (8×10^{11} ions/cm^2), offered the strongest multicolour photo-response and enhanced peak detectivity by more than one order at a low bias of operation. Annihilation of defects due to implantation was assumed to be the main cause for the better operational characteristics of the devices. Thus, it has been established successfully through the present study that low-energy light ion implantation can not only improve the material qualities of In(Ga)As/GaAs QD systems but also improve device performance.

References

1. A. Mandal, A. Agarwal, H. Ghadi, K.C. Goma Kumari, A. Basu, et al., More than one order enhancement in peak detectivity (D*) for quantum dot infrared photodetectors implanted with low energy light ions (H^-). Appl. Phys. Lett. **102**, 051105
2. R. Sreekumar, A. Mandal, S. Chakrabarti, S. Gupta, Effect of heavy ion implantation on self-assembled single layer InAs/GaAs quantum dots. J Phys. D: Appl. Phys. **43**, 505302 (2010)
3. R. Sreekumar, A. Mandal, S. Gupta, S. Chakrabarti, Effect of high energy proton irradiation on InAs/GaAs quantum dots: enhancement of photoluminescence efficiency (up to $\sim$7 times) with minimum spectral signature shift. Mater. Res. Bull. **46**, 1786–1793 (2011)
4. A. Mandal, U. Verma, N. Halder, S. Chakrabarti, The impact of monolayer coverage, barrier thickness and growth rate on the thermal stability of photoluminescence of coupled InAs/GaAs quantum dot hetero-structure with quaternary capping of InAlGaAs. Mater. Res. Bull. **47**, 551–556 (2012)
5. J. Suseendran, N. Halder, S. Chakrabarti, T. Mishima, C. Stanley, Stacking of multilayer InAs quantum dots with combination capping of InAlGaAs and high temperature grown GaAs. Superlattices Microstruct. **46**, 900–906 (2009)
6. J. Tatebayashi, N. Nuntawong, P.-S. Wong, Y. Xin, L. Lester, D. Huffaker, Strain compensation technique in self-assembled InAs/GaAs quantum dots for applications to photonic devices. J. Phys. D: Appl. Phys. **42**, 073002 (2009)
7. A. Stiff-Roberts, X. Su, S. Chakrabarti, P. Bhattacharya, Contribution of field-assisted tunneling emission to dark current in InAs-GaAs quantum dot infrared photodetectors. Photonics Technol. Lett. IEEE **16**, 867–869 (2004)
8. S. Chakrabarti, S. Adhikary, N. Halder, T. Aytac, A. Perera, High-performance, long-wave ($\sim$10.2 μm) InGaAs/GaAs quantum dot infrared photodetector with quaternary In0.21Al0.21Ga0.58As capping. Appl. Phys. Lett. **99**, 181102–181102-3 (2011)
9. S. Chakrabarti, X. Su, P. Bhattacharya, G. Ariyawansa, A.U. Perera, Characteristics of a multicolor InGaAs-GaAs quantum-dot infrared photodetector. Photonics Technol. Lett., IEEE **17**, 178–180 (2005)